

Interstellar Deuterium, Nitrogen, and Oxygen Abundances Toward BD +28° 4211: Results from the Far Ultraviolet Spectroscopic Explorer¹

George Sonneborn,² Martial André,³ Cristina Oliveira,³ Guillaume Hébrard,⁴
J. Christopher Howk,³ Todd M. Tripp,⁵ Pierre Chayer,^{3,6} Scott D. Friedman,³
Jeffrey W. Kruk,³ Edward B. Jenkins,⁵ Martin Lemoine,⁴ H. Warren Moos,³
William R. Oegerle,² Kenneth R. Sembach,³ and Alfred Vidal-Madjar⁴

ABSTRACT

High resolution far-ultraviolet spectra of the O-type subdwarf BD +28° 4211 were obtained with the Far Ultraviolet Spectroscopic Explorer to measure the interstellar deuterium, nitrogen, and oxygen abundances in this direction. The interstellar D I transitions are analyzed down to Ly ϵ at 920.7 Å. The star was observed several times at different target offsets in the direction of spectral dispersion. The aligned and coadded spectra have high signal-to-noise ratios (S/N = 50 – 100). D I, N I, and O I transitions were analyzed with curve-of-growth and profile fitting techniques. A model of interstellar molecular hydrogen on the line of sight was derived from H₂ lines in the *FUSE* spectra and used to help analyze some features where blending with H₂ was significant. The H I column density was determined from high resolution *HST*/STIS spectra of Ly α to be $\log N(\text{H I}) = 19.846 \pm 0.035$ (2σ), which is higher than is typical for sight lines in the local ISM studied for D/H. We found that $\text{D/H} = (1.39 \pm 0.21) \times 10^{-5}$ (2σ) and $\text{O/H} = (2.37 \pm 0.55) \times 10^{-4}$ (2σ). O/H toward BD +28° 4211 appears to be significantly below the mean O/H ratio for the ISM and the Local Bubble.

Subject headings: ISM: Abundances — Cosmology: Observations — ISM: Evolution — Ultraviolet: ISM — Stars: Individual (BD +28° 4211)

²Laboratory for Astronomy and Solar Physics, Code 681, NASA Goddard Space Flight Center, Greenbelt, MD 20771; george.sonneborn@gsfc.nasa.gov, oegerle@s2.gsfc.nasa.gov

³Dept. of Physics and Astronomy, The Johns Hopkins University, Baltimore, MD 21218; mandre, oliveira, howk, chayer, scott, kruk, hwm, and sembach @pha.jhu.edu.

⁵Princeton University Observatory, Princeton, NJ 08544; tripp and ebj@astro.princeton.edu.

⁴Institut d'Astrophysique de Paris, 98bis Blvd. Arago, 75014 Paris, France; alfred, hebrard, and lemoine@iap.fr.

⁶Primary affiliation: Department of Physics and Astronomy, University of Victoria, P. O. Box 3055, Victoria, BC V8W 3P6, Canada.

¹Based on observations made with the NASA-CNES-CSA Far Ultraviolet Spectroscopic Explorer. *FUSE* is operated for NASA by the Johns Hopkins University under NASA contract NAS5-32985.

1. INTRODUCTION

The abundance ratio of atomic deuterium to hydrogen (D/H) is a key diagnostic of light element production and the baryon-to-photon ratio (η) in big bang nucleosynthesis (BBN, Walker et al. 1991). Significant efforts in recent years to measure D/H in high redshift intergalactic gas have generally yielded values in the range $\text{D/H} = (2.5 - 4.0) \times 10^{-5}$ (O'Meara et al. 2001 and references therein).

In galaxies, D/H is an important indicator of chemical evolution (Audouze & Tinsley 1974; Boesgard & Steigman 1985; Tosi et al. 1998), as D is easily destroyed in stars ($^2\text{H} + p \rightarrow ^3\text{He} + \gamma$) at temperatures of only a few million degrees. In

fact, there are no known appreciable sources of D other than BBN. The interstellar medium (ISM), as the repository of stellar mass loss, holds the keys to unravelling the chemical history of D over the age of the galaxy. Measurements of atomic D/H in the ISM were first made by the *Copernicus* satellite toward bright OB stars within ~ 500 pc of the sun (Rogerson & York 1973; see Vidal-Madjar & Gry 1984 for a review). Significant progress had been made using the Hubble Space Telescope (*HST*) to obtain some precise D/H measurements in the local ISM (Linsky et al. 1998; Vidal-Madjar et al. 1998), but these have necessarily been limited to very low column density lines of sight ($N(\text{H I}) \sim 10^{18} \text{ cm}^{-2}$) where Ly α can be used to measure the D I column density.

The D/H ratio was measured at high spectral resolution ($\lambda/\Delta\lambda \sim 80,000$) with the Interstellar Medium Absorption Profile Spectrograph (IMAPS, Jenkins et al. 1988, 1999) toward three OB stars (δ Ori A, Jenkins et al. 1999; γ^2 Vel and ζ Pup, Sonneborn et al. 2000) first studied by *Copernicus*. These studies showed unequivocally that there is a large spread in D/H (factor of 3) on sight lines toward early type stars at distances of 300-500 pc. The IMAPS instrument was limited to observing very bright OB stars by its instrument design. At that time IMAPS could only observe the lower Lyman series through Ly ϵ $\lambda 937$ because its gratings were coated with lithium-fluoride (LiF).

FUSE provides a new capability to study the entire Lyman series (except Ly α) in much fainter stars than were possible with *Copernicus* or IMAPS, and hence D/H in the ISM within 200 pc can now be studied systematically for the first time. This is important because the lines of sight to nearby stars are usually simpler with less blending of different velocity components. *FUSE* has sufficient sensitivity to perform absorption line studies of white dwarfs as well as extragalactic objects. Both categories of targets were inaccessible to *Copernicus* or IMAPS. The study of D/H throughout the Galaxy is one of the primary objectives of the *FUSE* mission (Moos et al. 2000).

In this paper we report the analysis of D, N, and O abundances toward the O subdwarf BD +28° 4211 using high signal-to-noise (S/N) ratio spectra obtained with *FUSE*. BD +28° 4211 has a very high temperature ($\sim 82,000$ K), lies at

a distance of ~ 100 pc, and has a H I column density, $N(\text{H I})$, of $\sim 10^{20} \text{ cm}^{-2}$. This column density is much higher than those of the other LISM lines of sight studied previously for D/H, and very similar to that of the D/H sight lines studied by IMAPS. In this $N(\text{H I})$ regime the Lyman series shortward of Ly δ $\lambda 949$ is required to study $N(\text{D I})$.

Because a measurement of D/H requires both accurate $N(\text{D I})$ and $N(\text{H I})$, we use *FUSE* spectra to measure total column densities for $N(\text{D I})$, $N(\text{N I})$, and $N(\text{O I})$ and *HST*/STIS spectra of Ly α to measure $N(\text{H I})$. Even in the regime $N(\text{H I}) \sim 10^{20} \text{ cm}^{-2}$, the damping wings of Ly β and higher Lyman series transitions are too weak to obtain an accurate $N(\text{H I})$ measurement.

The observations and data processing are presented in §2 and the stellar atmosphere model and synthetic spectrum in §3. The measurement of $N(\text{H I})$ is discussed in §4. In §5 we describe the measurement of $N(\text{D I})$, $N(\text{N I})$, and $N(\text{O I})$ by curve of growth and profile fitting techniques, as well as the analysis of interstellar molecular hydrogen. This H₂ model is used in the D I, N I, and O I analysis. The paper concludes in §6 with a discussion of the results and a comparison with other recent D/H studies in the Galaxy.

2. OBSERVATIONS

BD +28° 4211 was observed by *FUSE* through the LWRS aperture ($30'' \times 30''$) on 2000 June 13 for 2192 s (ObsID=M1080901), 2000 July 16 for 16677 s (ObsID=M1040101), and 2000 September 19 for 7864 s (ObsID=M1040105). One MDRS aperture ($4'' \times 20''$) observation was made on 2000 July 17 for 24795 s (ObsID=M1040102). The first observation was a short exposure to establish the feasibility and safety of using BD +28° 4211 for the *FUSE* calibration program because its far-UV flux is very close to the bright limit of the *FUSE* detectors ($F_\lambda \sim 10^{-10} \text{ erg cm}^{-2} \text{ s}^{-1} \text{ \AA}^{-1}$). The subsequent observations were made for the purpose of testing the acquisition of data with the Focal Plane Assembly (FPA) offset to different positions along the dispersion direction as a technique to reduce fixed-pattern noise when the observations are later coaligned and added. This procedure and the results are discussed below. The *FUSE* instrument and its performance are described by Moos et al.

(2000) and Sahnou et al. (2000).

The data were obtained in “histogram” mode because of the high far-UV flux of the star. In this data acquisition mode a two-dimensional spectral image is accumulated on board, eliminating any timing information within individual exposures. The observations were split into four intervals of approximately equal exposure time, each with a different X-offset of the FPA. The exposure time required for the last two LWRs FPA positions was obtained in part during observation M1040101 and in part during observation M1040105. A shift in FPA X causes a corresponding shift in the location of the spectrum on the detector along the dispersion direction. The spectral shifts and exposure times are given in Table 1. The FPA is fixed for the duration of each exposure so that there is no loss in spectral resolution relative to an observation taken at a single FPA location. The offsets for the MDRS observations span a smaller range in FES X than those of the LWRs observations in order to provide sufficient margin in the FPA range of motion. This margin is needed so that MDRS pickups can properly adjust the FPA’s to correct for image motion caused by small rotations of the primary mirrors on orbital timescales. For further information on this image motion see Sahnou et al. (2000). The shifts caused by this image motion, together with shifts caused by similar rotations of the gratings, result in a distribution of shifts clustered about the mean offsets given in Table 1. Even for MDRS, these spectral offsets span a range roughly twice the width of typical interstellar absorption lines or of the high-frequency components of the detector fixed pattern noise.

Exposure durations varied from 430 s to 535 s in order to minimize Doppler smearing of the spectrum by satellite orbital motion so that there is no degradation of spectral resolution. Most of the LWRs exposures were obtained during orbital night when O I and N I airglow emission is absent and that of H I is significantly reduced. When exposures having both orbital night and day segments are considered, over 70% of the LWRs data was obtained during orbital night. Over 82% of the MDRS data was obtained at night.

The data were processed with the latest version of the FUSE calibration pipeline (CALFUSE v. 1.8.7). For each channel, data for each exposure were aligned by cross correlation and combined on

a common heliocentric wavelength scale. Part of the resulting spectrum for the LWRs observations is shown in Figure 1. The LWRs LiF co-added spectra have $S/N \sim 100$ per 0.05 \AA resolution element in the LiF channels and $S/N \sim 60$ in the short-wavelength silicon-carbide (SiC) channels. The S/N in the MDRS spectra of BD +28° 4211 are about 25% lower than for LWRs. These S/N levels are close to the photon-noise limits. The analyses presented in this paper uses primarily SiC channel spectra. Figure 2 shows small sections of the spectrum near several of the Lyman lines and demonstrates the high quality of our spectra. Our analysis of spectral features in the BD +28° 4211 co-added spectra indicates that the spectral resolution is consistent with $\lambda/\Delta\lambda \sim 20,000$, the nominal spectral resolution obtained by the FUSE instrument (Sahnou et al. 2000). It is evident from Figures 1 and 2 that airglow has a negligible effect on these spectra. Ly β is the strongest airglow transition in the FUSE band pass and the observed Ly β profile is only weakly affected. O I airglow, if present, would primarily effect the stronger transitions longward of $\sim 950 \text{ \AA}$, but the O I column density is determined from much weaker lines that are unaffected.

Figures 1-3 show that the saturated H I lines have non-zero residual flux (on the order of a few percent). The FUSE instrument has very low levels of scattered light (Moos et al. 2000, Sahnou et al. 2000), as shown by the zero flux level below the Lyman limit (see Fig. 1). The residual flux in the Lyman lines is probably the result of wings of the instrumental line spread function (LSF; see Kruk et al. 2001). The shape of the LSF and its potential effects on the line profile analysis is discussed further in §5.1.

3. STELLAR MODEL FOR BD +28° 4211

MacRae, Fleischer, & Weston (1951) reported the first spectral analysis of BD +28° 4211 and classified it as an extremely blue star with peculiar spectrum (Op). The optical spectrum of BD +28° 4211 attracted their attention because of its very blue continuum and the presence of Balmer and He II lines. Greenstein (1952) estimated the distance to BD +28° 4211 and found out that the star was a subdwarf. BD +28° 4211

is now classified as sdO, based on the study of Moehler et al. (1990), in which the class is defined as having He II and strong Balmer absorption lines. Although low resolution optical spectra show only these lines, high-resolution spectra reveal, in addition, many weak metal lines. Herbig (1999) obtained high-resolution optical spectra of BD +28° 4211 at the Keck I telescope and detected a significant number of narrow absorption and emission lines (C IV, N IV, N V, O IV, O V, and Si IV), and also emission cores in H α , H β , and He II $\lambda\lambda$ 6560, 5411, 4685 lines. Using the O IV absorption lines, Herbig (1999) set an upper limit on the star's rotational velocity, $v \sin i \leq 4 \text{ km s}^{-1}$. Even though BD +28° 4211 is a well-known spectrophotometric standard star in the ultraviolet and optical (see, e.g., Bohlin 1986; Massey et al. 1988), its atmospheric parameters were investigated only recently by Napiwotzki (1993), Werner (1996), and Haas et al. (1996).

Using H+He NLTE stellar model atmospheres, Napiwotzki (1993) tried to fit the Balmer line profiles in BD +28° 4211's optical spectrum with no success. He demonstrated that the effective temperatures obtained from fits of individual Balmer lines showed large discrepancies. This inconsistency, known as the Balmer line problem, was also observed in central stars of old planetary nebulae and DAO white dwarfs (see, e.g., Napiwotzki & Schönberner 1993; Napiwotzki & Rauch 1994; Bergeron et al. 1994). To overcome this problem, Napiwotzki (1993) modeled the He I λ 5876 line, as it is a very sensitive diagnostic of effective temperature (T_{eff}), and obtained $T_{\text{eff}} = 82,000 \text{ K}$ and $\log(\text{He}/\text{H}) = -1.0$. He also derived the gravity $\log g = 6.2$ from the higher Balmer lines.

By analyzing the optical spectra of BD +28° 4211 and the central star of the planetary nebula S216, Werner (1996) concluded that the Balmer line problem was caused by the omission or inadequate inclusion of metal opacities. For instance, he matched the Balmer lines (H α -H δ) of BD +28° 4211 combining Napiwotzki's (1993) parameters ($T_{\text{eff}} = 82,000 \text{ K}$, $\log g = 6.2$, and $\log(\text{He}/\text{H}) = -1.0$) and the improved Stark-broadened CNO line profiles. He demonstrated that the effect of this added opacities increased the temperature in the deeper layers of the atmosphere, and decreased the temperature in the superficial layers, therefore modifying the Balmer

line formation. He noted that the low Balmer series members cores are deeper as they are formed higher in the atmosphere, where the temperature is lower. On the other hand, the high Balmer series members were less affected because they originate from deeper layers of the atmosphere. This new temperature structure caused by the addition of more realistic metal line opacities resolved the Balmer line discrepancy. Interestingly, Bergeron et al. (1993) had reached a similar conclusion to that of Werner (1996) by analyzing the DAO white dwarf Feige 55 and using a LTE iron-blanketed model.

For the purpose of this study, we adopt the stellar atmospheric parameters determined by Napiwotzki (1993) as they are the best available. We compute a grid of H+He NLTE model atmospheres with the following atmospheric parameters: $T_{\text{eff}} = 78000 \text{ K}$, 82000 K , and 86000 K ; $\log g = 6.0$, 6.2 , and 6.4 ; and $\log(\text{He}/\text{H}) = -0.6$, -1.0 , and -1.4 . We also compute a metal-line blanketed model including the following chemical composition: H, He, C, N, O, Si, S, Fe, and Ni. We then compute a grid of synthetic spectra from Ly α to the Lyman limit using the TLUSTY program developed by Hubeny & Lanz (1995) and an upgraded version of the program SYNSPEC (I. Hubeny 2000, private communication), which incorporates the Lemke (1997) Stark broadening tables for hydrogen. We explored the model parameter space (T_{eff} , $\log g$, and $\log(\text{He}/\text{H})$) to evaluate the uncertainties in the stellar H I Lyman + He II Balmer line profiles. §4 describes in more details the use of stellar models to determine the H I column density.

The *FUSE* spectrum of BD +28° 4211 (Fig. 1) shows many stellar and interstellar lines. The stellar spectrum displays the Lyman series of hydrogen from Ly β up to Ly-9 and the He II Balmer series from 1084 Å up to at least 942 Å. The spectrum also contains many stellar lines of highly ionized species, such as C IV, N V, O IV, O V, O VI, Si IV, P V, S IV, S V, S VI, Fe VI, Fe VII, Ni VI, and Ni VII. The strongest lines are the N IV λ 923.15 sextuplet, S VI $\lambda\lambda$ 933.38, 944.52 doublet, N IV λ 955.33, and O VI $\lambda\lambda$ 1031.91, 1037.61 doublet. In order to identify potential blending of photospheric and ISM lines, we first performed an abundance analysis of BD +28° 4211's atmosphere and then calculated a synthetic spectrum using the

derived abundances. Figure 3 illustrates the comparison between the synthetic spectrum and the FUSE spectrum for the wavelength range 920–927 Å.

BD +28° 4211 has several strong, narrow metal lines in the *FUSE* range and that made it possible to register the wavelength scale of the stellar model with the observed spectrum. In particular, S VI λ 944.523 is seen in both SiC channels and has a deep, narrow core. We used this line to align the model with the spectra. As expected, the zero point wavelengths are different from channel to channel because it depends on the FPA position as well as the location of the star in the aperture. It varied between -60 km s^{-1} and $+60 \text{ km s}^{-1}$ in our data, although larger offsets were occasionally detected in the first year of *FUSE* operations (Sahnow et al. 2000). Once the wavelength offsets are corrected, the best estimate from the *FUSE* data of the velocity of the star relative to the ISM is $+34 \pm 6 \text{ km s}^{-1}$, a value that is consistent with our more accurate determination of $+31 \pm 2 \text{ km s}^{-1}$ from *HST* spectra (see below). We increased the error to $\pm 8 \text{ km s}^{-1}$ to take into account any remaining uncertainties in the *FUSE* wavelength calibration.

4. DETERMINATION OF THE H I COLUMN DENSITY

4.1. Hubble Space Telescope Observations

The determination of the interstellar H I column density along the sight line to BD +28° 4211 uses an extensive series of archival observations taken with the Space Telescope Imaging Spectrograph (STIS) on board the *HST*. The H I column density may in principle be determined using the *FUSE* observations of this star. However, most of the Lyman-series lines in the *FUSE* bandpass are on the flat part of the curve of growth. In addition, the damping wings of interstellar Ly β and Ly γ , the strongest H I transitions in the *FUSE* bandpass are significantly less prominent than those for Ly α and comparable in strength with the stellar H I + He II profiles. Therefore, the only reliable procedure for determining an accurate H I column density to BD +28° 4211 is by fitting the Lorentzian wings of the very strong Ly α line. As illustrated below, the interstellar H I profile is much stronger than its stellar counterpart.

BD +28° 4211 is a calibration source for STIS, and observations have been acquired over several years with the E140M echelle grating projecting the two-dimensional spectrum onto the FUV MAMA (Kimble et al. 1998; Woodgate et al. 1998). All data were taken through the $0''.2 \times 0''.2$ aperture and cover the spectral range $\sim 1150 - 1750 \text{ Å}$. This instrumental setup provides a spectral resolution $R \equiv \lambda/\Delta\lambda \sim 45,000$ ($\Delta v \sim 7 \text{ km s}^{-1}$ FWHM), although the line spread function for data taken through this aperture has significant power in broad wings that extend well beyond this width (see Figure 13.87 in the Cycle 9 STIS Instrument Handbook). We used eight such observations taken over the time period 1997 Sept. 19 to 2000 Nov. 10. Exposure times for the individual observations were in the range 350–1800 s. Figure 4 shows a coaddition of the data sets used in our analysis in the region near Ly α . This figure demonstrates the quality of the data and shows the importance of high spectral resolution for separating the numerous stellar and interstellar lines in this region.

4.2. Data Calibration and Reduction

The E140M data have been reduced using the CALSTIS pipeline by two different approaches in an attempt to uncover sources of systematic error. One used the pipeline as developed by the STIS Instrument Definition Team, the other the standard STSDAS pipeline distributed within IRAF (see Voit 1997). The CALSTIS pipeline removes an estimated dark level, applies a flat field, corrects small-scale distortions, identifies the spectral trace, removes scattered light, extracts the one-dimensional spectrum, and performs the wavelength and flux calibrations. We show below that both analysis approaches yield the same result.

The scattered-light removal process is among the most important, particularly for our purposes where we are interested in the large-scale wings of the Ly α profile. Because the strength of the echelle-scattered light can be significant in E140M spectra, the Bowers & Lindler algorithm (see Landsman & Bowers 1997; Bowers et al. 1998) was used to estimate and remove scattered light from the data in the pipeline procedures. We found that this algorithm does a good job of determining an appropriate zero-level, as evidenced by the small residual fluxes in the saturated cores

of strong lines (e.g., the Ly α profile shown in Fig. 4).

After extracting the spectrum, several echelle spectral orders in the regions adjacent to Ly α were combined using a weighted averaging scheme where the orders overlap. The flux calibration between orders seems good for the E140M data sets used here. Even so, there can be some small fluctuations in the final co-added spectrum due to mismatches at the edges of orders, although in general these can be masked out and do not significantly affect our analysis.

4.3. Analysis Methodology

The method for deriving the H I column density along this sight line follows Jenkins (1971) and subsequent work (see discussion, particularly of error analysis, in Vidal-Madjar et al. 1998; Howk, Savage, & Fabian 1999; Jenkins et al. 1999; Sonneborn et al. 2000). The distribution of optical depth, $\tau(\lambda)$, with wavelength for Ly α is given by the product of the absorption cross-section, $\sigma(\lambda)$, and the column density. For H I at Ly α this is:

$$\tau(\lambda) \equiv \sigma(\lambda)N = 4.26 \times 10^{-20} N(\lambda - \lambda_0)^{-2}, \quad (1)$$

where λ_0 is the Ly α line center at the velocity centroid of interstellar hydrogen. The H I column density is determined to be the one that best matches the above distribution of optical depth with the observed profile. This method only gives information on the total column of H I, since the details of the component structure are all within the strongly-saturated core of the Ly α line which spans a velocity range of ± 200 km s $^{-1}$. It is extremely unlikely that the damping wings are affected by low column density H I absorption features. Any H I absorber that could modify the shape of the damping wings would have to have a heliocentric velocity $|v| > 400$ km s $^{-1}$ (see Fig. 9 of Sonneborn et al. 2000). The broad damping wings of Ly α are not sensitive to the Doppler broadening parameter. We therefore have very little information about b from the Ly α analysis.

The derivation of $N(\text{H I})$ was performed with two independent, though similar, fitting procedures. Both vary the important free parameters, which for our purposes include λ_0 and $N(\text{H I})$, to minimize the χ^2 statistic between the model, after convolution with the instrumental LSF, and the

observed spectra (see, e.g., Jenkins et al. 1999). We note that the specifics of the LSF are relatively unimportant for $N(\text{H I})$ as large as is found on this sight line (see, e.g., Appendix A of Howk et al. 1999). This insensitivity includes the possible presence of the broad wings of the STIS E140M LSF mentioned above, which are on a much smaller scale than that of the H I absorption.

We applied masks to exclude obvious stellar and interstellar absorption features from the fit. We also avoided fitting the very deepest portion of the Ly α line core (effectively those regions with flux $< 10\%$ of the stellar continuum within $\sim \pm 2$ Å of the line center) because of the possibility that stellar lines may be unseen in this low signal-to-noise region of the spectrum.

The stellar atmosphere for this type of star also has broad Ly α + He II absorption. It is, therefore, important to account for the stellar continuum underlying the interstellar absorption in our fitting process. For this purpose we used the synthetic spectrum and stellar Ly α + He II line profile described in §3.

The computed stellar spectrum was shifted to a heliocentric velocity of $+20.2$ km s $^{-1}$, the radial velocity of BD +28° 4211, for comparison with the observed Ly α profile. We determined this radial velocity by measuring the velocities of prominent stellar lines in the STIS E140M observations, the average of which gives a heliocentric velocity of $v_{hel} = +20.2 \pm 0.8$ km s $^{-1}$. The quoted uncertainty is the 1σ standard deviation of the individual measurements about the mean and does not include the uncertainties in the STIS absolute wavelength scale, which probably correspond to ~ 1.6 to 3.2 km s $^{-1}$. This determination agrees well with the stellar radial velocity of $v_{hel} = +21.4 \pm 1.7$ km s $^{-1}$ derived by Herbig (1999), where we use the mean and 1σ standard deviation of his individual measurements. For comparison, the average velocity of interstellar material along this sight line is $v_{hel} \sim -9$ to -13 km s $^{-1}$ (stronger lines give more negative velocity components due to the presence of weaker components on the blue side of the interstellar profiles). The stellar radial velocity is well constrained, although we found that offsets from this best value as large as 5 km s $^{-1}$ have no effect on the derived H I column density.

The model stellar spectrum was scaled to best match the observed flux distribution using a second-order Legendre polynomial, the parameters of which are treated as free parameters in the fitting process. In general, the shape of the calculated stellar model far from line center fits the data relatively well. However, the adoption of a low-order polynomial correction to the synthetic stellar continuum allows for several possible systematic effects, including mis-matches between the observed spectrum and the model, slight redistribution of flux in the scattered light removal process, stellar atmospheric variability, and other properties of the detector and observations that could change the absolute flux distribution on Angstrom scales.

We also allowed for the effects of uncertainty in the flux zero point, treating it as a free parameter in the fit. This corrects for any small uncertainty in the background subtraction on scales of several Angstroms. The derived corrections to the flux zero point were always less than a percent or two of the continuum away from the line core.

Because of the possibility that the stellar Ly α profile could be variable, we fit separately each of the individual observations taken at different times. No evidence of variability was found. This is discussed in more detail below in our discussion of systematic uncertainties.

4.4. Results and Discussion of Systematic Uncertainties

Figure 4 shows the best fit interstellar H I profile on top of the coadded STIS observations. The final estimate for the H I column is $\log N(\text{H I}) = 19.846^{+0.036}_{-0.034}$, where the uncertainties are 95% confidence limits (2σ if Gaussian errors are appropriate) including systematic effects. This is an average of the results from the two $N(\text{H I})$ determinations, which differed by only 0.003 dex ($< 1\%$), and uncertainties, for which we adopted the larger of the uncertainty estimates.

The uncertainties in $N(\text{H I})$ given above include estimates of the statistical (random) and systematic uncertainties added in quadrature. Because of the high quality of the data and the strength of the Ly α damping wings, the systematics dominate the statistical uncertainties in our analysis. Given the importance of the systematic

uncertainties, we discuss several below and their impact on the $N(\text{H I})$ determination.

Stellar model uncertainties – The largest identified source of systematic uncertainty for $N(\text{H I})$ is the adopted stellar model. However, fits to the observed Ly α profile which use only a straight line continuum rather than a stellar model for normalization produce H I column densities that are larger by only +0.1 dex ($\sim 25\%$). This sets an upper bound on the magnitude of the uncertainties due to the stellar models.

The effects of imperfectly-known stellar atmospheric parameters on $N(\text{H I})$ were estimated by refitting the interstellar Ly α absorption profile using model atmospheres with the most extreme stellar properties that are still nominally consistent with the determination of the atmospheric parameters (see §3). For this purpose we chose those models with the strongest and weakest stellar Ly α absorption profiles from a grid of atmospheres covering a wide range in parameters: $\log \text{He/H}$ (−0.6 to −1.4), T_{eff} (78,000 to 86,000 K), and $\log g$ (6.0 to 6.4).

The $N(\text{H I})$ values derived in this way were treated as extrema corresponding to 95% confidence limits (2σ assuming Gaussian statistics) about the best-fit result. While this approach does not account for any uncertainties in our knowledge of the fundamental physics of stellar atmospheres or radiative transfer, the adopted extreme atmospheres encompass a sufficiently large range of parameter space that the effects of any subtle atmospheric physics are expected to be small in comparison to the uncertainties estimated in our approach. The uncertainties associated with the adopted stellar model and our allowance for stronger and weaker stellar Ly α profiles dominate the uncertainties in the $N(\text{H I})$ determination.

We note that the effects of line-blanketing within the model atmosphere will be much smaller than the effects of the extreme atmospheric parameters investigated above. We verified this assumption with appropriate model calculations, and that the variation in the stellar Ly α profile occurs primarily in the core of the line where the residual flux in the observed spectrum is zero.

Residual scattered light – In principle, residual scattered light in the STIS E140M spectra could bias the $N(\text{H I})$ determination. The core of Ly α

is indeed very near zero, and we allowed the true flux zero point to vary as a free parameter in the fits. However, if light were distributed in the line wings in an appropriate way during the scattered light removal process, this could potentially be a source of systematic uncertainty in our H I column density determination.

As a check of the $N(\text{H I})$ value derived from STIS E140M observations, we also analyzed archival observations taken with the pre-COSTAR Goddard High Resolution Spectrograph (GHRS) first-order G160M grating through the small science aperture ($0''.25 \times 0''.25$). These spectra have a resolution of $\sim 15,500$ ($\sim 19.3 \text{ km s}^{-1}$ FWHM). While the observations do not cover the entire extent of the red wing of Ly α , the holographically-ruled G160M grating had excellent scattered light properties (Cardelli, Ebbets, & Savage 1993). Eight observations with a total exposure time of 1152 s were reduced and combined using procedures described by Howk et al. (1999). From these spectra we found $\log N(\text{H I}) = 19.842 \pm 0.020$ (2σ , statistical uncertainties only). This value is so close to the value derived using the STIS E140M observations that we believe residual scattered light uncertainties are not likely to be a significant source of error.

Stellar atmospheric variation – The atmospheric profile of the star could be variable, and there is some evidence that BD+28° 4211 may be part of a binary system (see Napiwotzki 1999; Massey & Gronwall 1990). To account for the possibility that the stellar Ly α profile might vary, we separately calculated the best-fit H I column densities for each of the eight individual STIS observations. The dispersion in these best-fit measurements for the ensemble of observations was small and was added in quadrature to the final uncertainty estimate. The dispersion of the individual measurements about the mean was much smaller than that resulting from the variation of stellar model parameters described above.

5. COLUMN DENSITIES OF ATOMIC DEUTERIUM, NITROGEN AND OXYGEN

5.1. General Considerations

Both curve of growth (COG) and profile fitting techniques were used to determine $N(\text{D I})$ and

$N(\text{O I})$ in order to better understand potential sources of systematic error. Profile fitting alone was used for $N(\text{N I})$ because there are only three unsaturated and unblended N I lines available (the $\lambda 952$ multiplet). The *FUSE* spectra were also analyzed to develop a model for interstellar $N(\text{H}_2)$ for rotational levels $J = 0 - 4$. The comparison of measurements from multiple channels (SiC1 and SiC2) and observations (LWRS and MDRS) is a powerful tool that improves our statistics and helps to identify poor data quality due to instrumental effects.

In the COG method the equivalent width, W_λ , of several lines of the same species having different oscillator strengths are measured and their distribution in the $\log(W_\lambda/\lambda) - \log(Nf\lambda)$ plane is compared with a theoretical curve of growth for a single absorption component subject to a Maxwellian velocity distribution. The free parameters in the fit are the column density, N and Doppler spread parameter, b . However, if there is a complex velocity distribution, b is regarded as an “effective” Doppler spread and as such has no physical meaning. Continuum placement and equivalent width measurements are treated in independent steps and assume some a posteriori conservative error bars to take into account the uncertainties in continuum placement. The COG method is potentially vulnerable to error because of the assumption of a single-component profile. In particular, at the *FUSE* spectral resolution narrow, unresolved components could be concealed by broader features, which could result in underestimated column densities (Nachman & Hobbs 1973, Savage & Sembach 1991). Jenkins (1986) showed that column densities accurate to $\sim 10\%$ can be obtained with the COG method provided that the lines are not heavily saturated ($\tau_0 \leq 2$) and have smooth distributions of b and τ in their components. In the case where all transitions are on the linear part of the COG, the column density is insensitive to the line-of-sight velocity structure. One of the advantages of the COG method is that it is not too sensitive to the LSF. On the other hand, transitions blended with lines from other species should be avoided in this analysis technique. In this case, profile fitting may be more appropriate.

The profile fitting method makes the same basic assumptions as the COG: an interstellar absorption line is formed in a single component and is

described by two parameters: N and b . In addition the wavelength centroid of the line, or radial velocity, v_r , is also a free parameter. The fitting technique also assumes that each interstellar component produces absorption lines described by Voigt profiles. We note that in our analysis the Doppler parameter, b , has no unique physical interpretation. Normally $b^2 = 2kT/m + v_{turb}^2$. However, from the *FUSE* spectra alone, with spectral resolution of $\sim 15 \text{ km s}^{-1}$, temperature (T) and turbulent motion (v_{turb}) effects on the line widths are not easily separated. We can, however, use b to set an upper limit on T .

Lines of sight with multiple components are often more reliably analyzed with a fitting technique than it is with the COG. In practice, to fit a multiple-component COG requires a prior knowledge of v_r and b for each component as well as their expected relative ratios. This information is not necessary with profile fitting because in principle it lies in the profiles. For the same reason, the blending of adjacent lines is also easier to model with a fitting procedure.

A second significant advantage of our profile fitting analysis is that absorption lines and continua are fit simultaneously so that continuum shape and placement are treated as free parameters. We have used the profile fitting program `Owens.f` (Lemoine et al. 2001, Hébrard et al. 2001). `Owens.f` is a powerful profile fitting program that simultaneously models multiple spectral lines, species, and absorption components in an arbitrary number of spectral regions, or windows. Many quantities characterizing the fit may be treated as free or fixed parameters (N, T, v_{turb} , LSF, continuum placement and shape, background level, velocity offset between spectral windows, etc.). The program uses an optimized χ^2 -minimization algorithm to obtain fast convergence. The flexibility of `Owens.f` allowed us to analyze many different cases. As with any convergence algorithm, parameter space was explored to verify that a converged solution was the true minimum and not a local minimum far from the true solution. This was done by changing the initial parameters and/or conditions and then running the program again to reach a new converged solution. A potential disadvantage of profile fitting is that knowledge of the instrument LSF is required, and errors in the assumed LSF have the

potential to bias the results.

The instrumental LSF is a key parameter in the profile fitting analysis of interstellar absorption lines. The characterization of the *FUSE* LSF was incomplete at the time of this analysis (see Kruk et al. 2001). Although there is evidence that the *FUSE* LSF has wings that effect the zero level of heavily saturated lines (§2), two independent analyses (Hébrard et al. 2001, Wood et al. 2001) show that modelling of weak unsaturated lines with a single Gaussian LSF and a double Gaussian LSF give very consistent results within the uncertainties of the *FUSE* LSF parameters (see the companion papers referenced above for further details). For our profile fitting analyses we used a single gaussian LSF for each component modelled.

In the next subsection the interstellar H_2 model is derived. The following subsections describe the COG analysis of D I and O I and the profile fitting analysis of D I, O I, and N I.

5.2. Interstellar H_2 Column Densities

The *FUSE* spectra of BD +28° 4211 contain a large number of absorption lines from interstellar molecular hydrogen. Absorption arising from H_2 rotational levels $J = 0 - 4$ can be clearly seen along this line of sight. Many H_2 lines are blended with stellar and other ISM features. For transitions corresponding to the rotational level $J = 4$ there are not enough unblended lines to derive a reliable column density using either COG or profile fitting techniques. However, a 3σ upper limit for $N(\text{H}_2) J = 4$ is derived. A few H_2 transitions from $J = 5$ and 6 may also be present. The best candidate is Werner 0 - 0 Q(5) at 1017.831 Å. However, the *FUSE* spectra of BD +28° 4211 contain many unidentified stellar features and it is possible that this and other weak transitions could be stellar in origin, or if actual H_2 ISM lines, blended with stellar lines. Due to these uncertainties, the column densities for $J \geq 5$ could not be estimated. The H_2 column densities for rotational levels $J = 0 - 3$ were measured using both profile fitting and COG methods, using lines that appeared free of blending, as judged by the shape of the absorption profile and with the help of the stellar model.

Profile fitting used only unsaturated lines, i.e.

lines for which the absorption profile deconvolved with the LSF did not have a residual intensity in the line core < 0.1 . The column density for each rotational level was determined independently. The synthetic stellar spectrum gave guidance when selecting the H_2 lines to be analyzed in order to avoid blending with stellar features. Each spectral region (several Angstroms) was first normalized with a spline function. A subset of this region, a spectral window of $\sim 1\text{\AA}$, was used by `Owens.f` where a polynomial (up to 4th order) was fit to the continuum away from the line. We restricted the size of the spectral windows used in the `Owens.f` analysis because of concern about small nonlinearities in the *FUSE* wavelength calibration on larger scales. The number of lines analyzed for each J level are listed in Table 3. All the H_2 lines analyzed lie away from the H I lines. The background was set to zero for each window. The width of the Gaussian LSF was free to vary from window to window and between successive fits. Once the best fit was found, corresponding to a minimum χ^2 , the error in the column density was calculated by fixing $N(H_2)$ to a different value and computing a new optimized fit, which always had a larger χ^2 . The difference of the new reduced χ^2 from χ^2_{min} determined the 1, 2, 3, 4, 5, 6, and 7 σ deviations from the best fit. The adopted 1 σ error was the average of these values to allow for any asymmetry in the $\Delta\chi^2$ curve. Only an upper limit was derived for $N(H_2)$ $J = 4$, the result of its weak transitions being indistinguishable from weak stellar features. $N(H_2)$ and 2 σ errors derived this way are given in Table 3.

The H_2 equivalent widths were measured by directly integrating the area of several lines for each rotational level for $J = 0 - 3$. The continuum near each line was defined by a Legendre polynomial up to 5th order. W_λ of each transition is the weighted average of W_λ measured in each channel where the line was present. A single-component Gaussian COG was fit to the data for each rotational level, and the residuals about the best-fit curve were minimized (Figure 5). The resulting column densities are completely consistent with the profile fitting results, although with somewhat larger uncertainties. Assuming the population of the lower rotational states of H_2 is determined by collisional excitation and a Boltzmann distribution, the excitation temperatures are $T_{1,0} = 313\text{ K}$, $T_{2,1} = 294$

K and $T_{3,2} = 296\text{ K}$. However, the similarity of $T_{i,j}$ for $J = 0 - 3$ indicates that one or more of these assumptions may not be correct. The uncertainty in $N(H_2)$ $J = 0$ may permit a more typical value of $T_{1,0} \sim 100\text{ K}$. The total H_2 column density is $\log(N(H_2)) = 15.13^{+0.20}_{-0.08}\text{ cm}^{-2}$.

5.3. D I and O I Curve-of-Growth Analyses

The high S/N of the *FUSE* observations of BD+28°4211 permits analysis of the D I transitions down to 916 Å where the H I profiles start to overlap. However, some of the higher D I Lyman series lines (916–918 Å) have strengths that vary significantly from line to line and channel to channel. These inconsistencies probably originate in the fixed pattern noise of the detector and/or in blends with weak stellar features or interstellar H_2 . Therefore, the COG analysis of D I was limited to the six transitions listed in Table 4. Most of the D I lines (Ly γ – Ly η) lie in the blue wing of the corresponding H I lines. Four out of the six transitions fall on the linear part of the curve of growth. Hence, the velocity structure on the line of sight does not influence the final column density estimate (see §5.4).

5.3.1. D I Continuum Normalization

The stellar H I and He II and interstellar H I absorption profiles dominate the shape of the continuum near the D I feature. A continuum model was constructed, where the key parameters are $N(H\text{ I})$, $N(H_2)$, and b for the ISM model computed with `Owens.f` and T_{eff} , $\log g$ and He/H for the stellar model. We adjusted the stellar plus interstellar model to fit the data (a small zero-point shift in the model’s wavelength scale and scaling the absolute flux of the model to match the observed flux level – see Fig. 3). These are discussed further below.

The stellar model has been discussed in detail in §3. The uncertainties in T_{eff} and $\log g$ considered in the $N(H\text{ I})$ analysis ($\sim 5\%$) have a negligible effect on the shape of the H I + He II profile near the D I lines we are studying. While varying these parameters would change the goodness of the fit far from the core of the D I lines, the continuum placement would be similar. As to the He/H ratio, this affects only the two strongest lines (D I Ly

and Ly δ) where He II is readily apparent in the model.

The overall shape of the model agrees well with the spectrum, although we noted some localized discrepancies. The different spectra showed flux scale differences from the model of up to +5% for LWRS and +10% for MDRS. The latter suffered from small variations in slit transmission due to mirror motion (see Sahnou et al. 2000) and a small part of the flux was lost in this process. The MDRS flux calibration is also less well known than that of the LWRS channel.

We modelled the interstellar H I profiles by using `Owens.f` to fit the relevant H I Lyman series transitions (919 – 972 Å), forcing the column density to $\log(N(\text{H I})) = 19.85$ and the adopted the $N(\text{H}_2)$ parameters from Table 3. A one-component fit agreed well with the data. A three-component fit was also performed (cf. §5.4) but there was no improvement in the fit because in H I these components are buried in the saturated line cores. The purpose of this H I model was to find a good empirical match with the data to assist in the measurements of D I W_λ , not to determine $N(\text{H I})$.

5.3.2. W_λ Measurements

The general method for measuring W_λ for the D I lines is illustrated in Figure 6. First, the data were divided by the stellar model appropriately registered in λ and F_λ (Fig. 6a and d). This process sometimes produced what was judged to be a poor fit in the red wing of interstellar H I, especially for D I $\lambda 925$. We believe this is due to differences in the number, location, and strength of weak stellar lines between the blue and red wings. In spite of the concern about such line blanketing differences, W_λ for D I $\lambda 925$ is consistent with the other D I transitions analyzed.

Second, the normalized spectrum was then corrected for interstellar H I (Fig. 6b and e) by using the H I model profiles described above. W_λ of each D I feature was measured by fitting a Gaussian to the residual D I absorption line (Fig. 6c and f) using all of the profile except the far red wing of where the near-zero flux near the line core of H I produces large residuals. Since the principal source of error in this analysis is the stellar continuum placement, we adopted a conservative

approach, scaling the continua by $\pm 3\%$ and re-measuring W_λ . This produced noticeably poor fits that represent extreme cases. We assumed that these fits were 2σ from the best fit. Therefore, the $N(\text{D I})$ errors include the systematic error due to continuum placement.

Table 4 gives the D I W_λ values for each channel and aperture. There are four independent measurements of W for each DI transition (SiC1 and SiC2, LWRS and MDRS). These measurements were consistent to within 1σ , except for the three cases where W_λ was omitted. These measurements were discarded because they were inconsistent (discrepant by $\geq 50\%$) with the other measurements of the same transition. We concluded that these cases were probably caused by detector artifacts (fixed-pattern noise) after careful comparison of line profiles in the four aperture and channel combinations. The far right hand column in Table 4 is the mean W_λ used in the COG. The COG fit for D I is shown in Figure 7. We found $\log N(\text{D I}) = 14.99 \pm 0.10$ (2σ) and $b = 5.2 \text{ km s}^{-1}$.

5.3.3. O I Curve of Growth

A curve of growth was constructed for O I, for each segment (SiC1 and SiC2, MDRS and LWRS), using the lines and f -values of Table 4. O I $\lambda\lambda 924.52$, 936.63, and 950.88 were not used because of blending with stellar or H₂ features. The general procedure to construct the curve of growth is similar to what was described above for the H₂ COG analysis (§5.2). For the O I COG we chose lines that are free of blending with other ISM or stellar features. Unlike D I and H₂, O I f -values may have relatively higher uncertainties in the *FUSE* bandpass, all of them coming from theoretical calculations (Morton 1991; Morton 2000, private communication; Verner, Barthel, & Tytler 1994). Unlike the pathological case of O I $\lambda 1026.5$ pointed out by Jenkins et al. (2000), the other O I f -values appear to be self-consistent. W_λ and associated errors measured for the four spectra are listed in the Table 4. The COG fit to the mean W_λ is shown in Figure 8 and the derived column densities are given in Table 5. A COG fit to the weighted average of W_λ for the different channels and apertures yields $\log N(\text{O I})_{\text{COG}} = 16.23 \pm 0.08 \text{ cm}^{-2}$ (2σ) and $b = 4.5 \text{ km s}^{-1}$.

5.4. Profile Fitting Analysis

A profile fitting analysis of D I, N I, and O I column densities was performed to provide a comparison with the results of the COG analysis in the previous subsection. The general technique is identical to that discussed in §5.2. Since `Owens.f` was used to fit D I, N I, and O I simultaneously, the following discussion also applies to $N(\text{O I})$ and $N(\text{N I})$.

The five D I transitions analyzed ($\text{Ly}\epsilon$, $\text{Ly}\zeta$, $\text{Ly}\eta$, $\text{Ly}\theta$, and $\text{Ly}\iota$) are not saturated. With the use of a fitting procedure, the choice of the lines to analyze is different than with the COG technique. An example is $\text{Ly}\zeta$ which was not used in the COG analysis because it is blended with H_2 $J = 1$ and $J = 2$. By adopting the H_2 solution (Table 3) as a constraint in the fit, this transition is now part of the fitting analysis and easily deblended from the H_2 . We note that the errors in $N(\text{H}_2)$ are not significant for the $N(\text{D I})$ analysis because the H_2 lines blended with $\text{Ly}\zeta$ are on the flat part of the COG. The two strongest D I transitions used for the COG ($\text{Ly}\gamma$ and $\text{Ly}\delta$) were omitted from the profile fits because they are mildly saturated ($\tau_0 \sim 2$). Uncertainties in our knowledge of the *FUSE* LSF could influence the results derived from profile fits to such lines. In any case, $N(\text{D I})$ is well constrained by the other five transitions.

Although the continuum close to the O I lines is very smooth and easily fit with a low-order polynomial, some of the O I transitions used in the COG are indeed saturated and for this reason they were not included in the $N(\text{O I})$ profile fitting analysis using `Owens.f`. Only three O I transitions were used to determine $N(\text{O I})$: 919.92 Å, 925.45 Å, and 930.26 Å. The strongest of these has $\tau_0 \sim 1$.

There are many N I transitions in the *FUSE* range and four multiplets are detected: $\lambda\lambda 952$, $\lambda\lambda 953$, $\lambda\lambda 964$, and $\lambda\lambda 1134$. The 952 Å triplet is free of any blending with H_2 or ISM atomic lines and seems clear of stellar features. Since all the lines of this triplet are still on the linear part of the curve of growth, deriving the column density is straightforward. This is not the case for the $\lambda\lambda 953$, $\lambda\lambda 964$, or $\lambda\lambda 1134$. These multiplets are all saturated and much less sensitive to N than they are to b . The 964 Å triplet is the next strongest after $\lambda\lambda 952$, but these lines are blended with several H_2 lines, P II $\lambda 963.8$, and

with unidentified stellar features. With only one multiplet ($\lambda\lambda 952$) we did not perform a COG analysis of N I. The N I f -values used were provided by D. Morton (2000, private communication).

The `Owens.f` analysis of the D I, N I, and O I lines allow many quantities that characterize the fits to be treated as free parameters. These include the wavelength and flux zero points of each profile, the polynomial coefficients for each spectral window, the LSF parameters (discussed below), the column densities N , and Doppler parameters b . In total, there were about 40 spectral windows and about 1500 degrees of freedom to fit 11 transitions. The H_2 column densities (Table 3) were adopted as a fixed constraint. We fit the five lines of D I, three of O I, and three of N I in the four data sets simultaneously, providing a global solution.

The continuum for the D I line profiles was determined by a different approach than was used for the D I W_λ measurements. There is sufficient information immediately adjacent to the D I features to establish the continuum with a polynomial without normalizing the spectrum or modelling the stellar and interstellar H I. The shoulder of the blue wing of the interstellar H I profile, excluding the D I feature, was fit by a 4th order polynomial. Examples of the continuum and D I profile fits are shown in Figure 9. The effective b is not tightly constrained in this analysis because the true shapes of the D I profiles are unresolved for these weak lines.

The effect of simultaneously modelling the interstellar H I and D I profiles and fitting a polynomial to the stellar contribution alone was also examined. The line-of-sight velocity structure becomes critical when higher Lyman series of D I and H I are fit together. In this case for BD +28° 4211 the effective b is dominated by H I and is larger than the D I effective b , much larger than the expected $\sqrt{2}$ difference between H and D. This is probably the result of very weak H I components not visible in D I or any other species that become a factor in the width high Lyman series profiles of H I. Overestimating b for D I leads to an anomalously low $N(\text{D I})$. When D I and H I are fit together a larger fitting window ($\Delta\lambda \sim 4$ Å) is also required, forcing D I to be shifted from its true center as a result of small residual nonlinearities in the *FUSE* wavelength calibration. Due to the introduction of these systematic errors we

rejected this fitting approach in favor of the techniques described in the previous paragraph and illustrated in Figure 9.

The influence of the LSF assumptions and the velocity structure were carefully examined. Three cases were considered in the profile fitting analysis. One way of investigating the sensitivity of the fit to the assumed LSF was to let *Owens.f* adjust it as part of the χ^2 minimization. For Case 1 we considered a fixed LSF associated with each channel/aperture combination, ignoring the possible variations with wavelength. The choice of the LSFs was made after several *Owens.f* test runs with different parameters. In Case 2, we assumed a LSF modeled by a single Gaussian with FWHM that varied freely with wavelength and from channel to channel. Case 3 examined the effect of line-of-sight velocity structure as derived from STIS Fe II profiles on the derived column densities. The continuum was determined in all three cases by the technique illustrated in Figure 9. For all three cases, the LSF was modelled as a single Gaussian for reasons discussed at the end of §5.1.

A free LSF (Case 2) clearly improved the fit, as indicated in Table 6, compared with the fixed LSF (Case 1). Only a few spectral windows showed LSF width variations as large as 20% (≤ 2 pixels). Such variations may be the result of fixed pattern noise that is only partly corrected by means of the FP-split procedure, or from weak, unresolved photospheric features. For Case 2 the reduced χ^2 was slightly lower than before but the $N(\text{D I})$ and $N(\text{O I})$ were unchanged. The fit of the N I lines, fit simultaneously with D I and O I, showed slight differences but are within the 2σ uncertainty. Although the LSF calibration as a function of λ , channel, and aperture is not yet well determined (Kruk et al. 2001), we accounted for this by considering two extreme assumptions (free vs. fixed LSF) and adopting an average column density that includes this systematic effect in the errors.

For Case 3 we used high resolution STIS E230H spectra to provide resolved Fe II $\lambda\lambda 2344, 2382$ line profiles, the only Fe II lines available in the existing archival high resolution spectra of BD+28°4211. Profile fits to the STIS spectra alone found three components at $v_{hel} = -2.4, -9.7$, and -17.0 km s^{-1} (listed in order of decreasing Fe II column density) and a total Fe II column density of $\log N(\text{Fe II}) = 13.81 \text{ cm}^{-2}$

(see Figure 10). We also performed a simultaneous fit of *FUSE* and STIS data using *Owens.f*. This fit found the velocity separations of the three components to be 3.5 and 10.9 km s^{-1} and $\log N(\text{Fe II}) = 13.79 \text{ cm}^{-2}$, compared with 7.3 and 7.3 km s^{-1} for the STIS data alone. These differences (3 – 4 km s^{-1}) reflect the level of uncertainty of these fits.

For the Case 3 fits, the relative ratios of each component for the neutral species was very different from that in Fe II. Specifically, the weakest (bluest) Fe II component had no contribution from D I, N I, or O I. This could be due to ionization effects or iron might be depleted in different ways in different environments, while N I and O I are only lightly depleted (Savage & Sembach 1996). It appears that the fit of the neutral species suffered from the use of the Fe II lines, showing a higher reduced χ^2 . We believe that the neutral species are not fit well by the Fe II velocity structure because the b -values and/or the velocity structure appears to be different. Since we do not resolve the component structure with *FUSE*, we rely on the one component solution for D I, N I, and O I.

The column density errors were calculated by computing new fits for different fixed values of N away from the best fit column density and deriving $\Delta\chi^2$ as a function of N . The 3σ error is given by $\Delta\chi^2 = 9$. The average gives $\log N(\text{D I}) = 14.99 \pm 0.03 \text{ cm}^{-2} (2\sigma)$.

The COG and profile fitting analyses give the same D I column density and have error estimates that differ only slightly at the 2σ level. It is reassuring that both approaches give results within 5% of each other. The errors from the COG analysis are more conservative than the ones coming from the profile fits. The reason for this is that moving the continuum by $\pm 3\%$, as was done for the COG, we have probably overestimated the errors. Yet they seem to fairly reflect the scatter seen in the individual W_λ measurements. Combining the results, we adopted a straight average of $N(\text{D I})$ from the COG and profile fitting analyses and arrive at the final D I column density $\log N(\text{D I}) = 14.99 \pm 0.05 \text{ cm}^{-2} (2\sigma)$ for the BD+28°4211 line of sight.

Figure 11 compares the O I fits for SiC2 spectra from the LWRS and MDRS observations. Combining the results from the different LSF approaches (see Table 6) gives $\log N(\text{O I}) =$

$16.21 \pm 0.10 \text{ cm}^{-2}$ (2σ) from the profile fitting analysis.

Most of the O I lines used in the profile fitting analysis are close to saturation which may make both this and the COG method sensitive to the velocity structure. We investigated this possibility by analyzing the effect of a three-component velocity structure on the COG analysis. The goal of this investigation was to see if a one-component COG could still be applied with success on this line of sight. We computed a model for the line of sight for D I and O I lines with three components as seen in the STIS Fe II profiles. Performing a one-component COG analysis of the model line profiles yielded D I and O I column densities within 5% of the model and an average effective b of 5.8 km s^{-1} . Although the velocity structure found in Fe II is not identical to that for the neutral species, it is the best available. For the BD +28° 4211 line of sight a one-component COG gives reliable results. We find that the effective b from the analysis of the three-component simulated profiles is consistent with the effective b from the analysis of the actual data. The final value adopted for the O I column density is $\log N(\text{O I}) = 16.22 \pm 0.10 \text{ cm}^{-2}$ (2σ).

Examples of the fits to the N I $\lambda\lambda 952$ lines are shown in Figure 12 and the results listed in Table 6. The mean fit gives $\log N(\text{N I}) = 15.55 \pm 0.13$ (2σ).

6. RESULTS AND DISCUSSION

The abundances derived in the previous sections are summarized in Table 8 along with their ratios. The 2σ errors in the abundance ratios are those from the individual column densities combined in quadrature. We find that $\text{D/H} = (1.39 \pm 0.21) \times 10^{-5}$ (2σ) toward BD +28° 4211. Götz et al. (1998) observed BD +28° 4211 with the Tübingen echelle spectrograph ($\lambda/\Delta\lambda \sim 10,000$) on the *ORFEUS-SPAS II* mission and found $\text{D/H} = (0.8^{+0.7}_{-0.4}) \times 10^{-5}$ (1σ). Our result is at the upper end of their range. The *FUSE* result for BD +28° 4211 is just marginally consistent with the higher D/H value found for the more distant sight line toward Feige 110 ($\text{D/H} = (2.1 \pm 0.70) \times 10^{-5}$) by Friedman et al. (2001). The total neutral gas column toward BD +28° 4211 is very similar to that toward $\gamma^2 \text{Vel}$, ζPup , and

$\delta \text{Ori A}$ (at distances of 250–500 pc), the sightlines studied with IMAPS to measure D/H (Jenkins et al. 1999, Sonneborn et al. 2000). D/H toward BD +28° 4211 is in the middle of the range of values found in the IMAPS studies.

Our result for D/H toward BD +28° 4211 is similar to values found on lines of sight in the Local Bubble by *FUSE* (Moos et al. 2001) and *HST* (Linsky et al. 1998), even though BD +28° 4211 lies just outside the Local Bubble. The total H I column density toward BD +28° 4211 is $\log N(\text{H I}) = 19.85$, much higher than the other LISM sight lines studied thus far by *FUSE* for D/H (except for Feige 110). The Na I contours for the LISM (Sfeir et al. 1999) show that BD +28° 4211 is located in a region of higher column density just beyond the edge of the Local Bubble, with much lower densities in the intervening $\sim 100 \text{ pc}$. The H I column toward BD +28° 4211 is large enough that the local cloud is a negligible contribution. Our abundance measurements are therefore dominated by the gas $\sim 100 \text{ pc}$ from the Sun. As discussed by Moos et al. (2001), there is now considerable evidence for a constant D/H within the Local Bubble. Beyond $\sim 100 \text{ pc}$, however, or more specifically outside the Local Bubble and $\log N(\text{H I}) \geq 19.5$, there appears to be a considerable spread in D/H as larger amounts of gas are probed.

The total H_2 column density is $\sim 1.3 \times 10^{15} \text{ cm}^{-2}$, and the molecular fraction $f(\text{H}_2) \sim 3.8 \times 10^{-5}$. This low value of $f(\text{H}_2)$ is typical of lower H I column density ISM sight lines (Tumlinson et al. 2001). The abundance of H_2 at $\sim 100 \text{ pc}$ indicates that some molecular gas is present, but the low column densities and high excitation temperature are consistent with a low density environment where UV pumping is probably significant.

The profile fitting and COG analyses for D I and O I consistently found an effective b -value of $\sim 5 \text{ km s}^{-1}$. Although *FUSE* lacks the spectral resolution to separate thermal and non-thermal effects on the neutral gas line profiles, we can set an upper limit to the temperature. For D I $b = 5.0 \text{ km s}^{-1}$ corresponds to $T \leq 6000 \text{ K}$. For O I, however, the same b corresponds to $T \leq 40,000 \text{ K}$. There must either be a significant non-thermal contribution to the line broadening of the neutral species, or the component structure on the BD +28° 4211 line of sight has a significant effect

of the line shapes. Very high resolution spectra of species such as Na I are needed to determine the component structure, T and v_{turb} of the neutral gas as a function of velocity.

The O/H ratio toward BD +28° 4211 is $(2.37 \pm 0.55) \times 10^{-4}$ (2σ), a value that is anomalously low with respect to the Local Bubble and the ISM. The BD +28° 4211 O/H is marginally consistent with the mean O/H ratio in the ISM ($\langle O/H \rangle_{ISM}$) of $(3.19 \pm 0.28) \times 10^{-4}$ (2σ) found by Meyer et al. (1998) in a study of O I $\lambda 1355$ on 13 sight lines toward OB stars at distances of 130 – 1500 pc. Recently, however, Meyer (2001) updated $\langle O/H \rangle_{ISM}$ to $(3.43 \pm 0.28) \times 10^{-4}$ as a result on a revised f -value for the $\lambda 1355$ transition. The *FUSE* O/H ratio toward BD +28° 4211 is well outside the estimated uncertainties in the revised $\langle O/H \rangle_{ISM}$. In the Local Bubble $\langle O/H \rangle_{LB} = (3.9 \pm 0.3) \times 10^{-4}$ (1σ) (Moos et al. 2001), slightly higher than Meyer’s revised value for the ISM, although consistent within their respective uncertainties. Moos et al. (2001) also finds the same value of the mean O/H when the more distant sight line to Feige 110 is included. Of the five sight lines for which O/H is measured by *FUSE*, only BD +28° 4211 gives a value that disagrees with $\langle O/H \rangle_{ISM}$ and $\langle O/H \rangle_{LB}$. If correct, the gas just outside the Local Bubble has a low O abundance. This implies that the gas toward BD +28° 4211 beyond the Local Bubble would appear to have a different chemical history than that sampled in the Meyer et al. study.

We have searched for other possible explanations for the low O/H ratio toward BD +28° 4211. O I is not vulnerable to ionization effects (Jenkins et al. 2000), so the O I-to-H I ratio should accurately reflect the total O/H abundance ratio. If the error is in the H I column density, then correcting O/H to obtain agreement with $\langle O/H \rangle_{ISM}$ would result in a large D/H ratio ($\sim 2.0 \times 10^{-4}$). Such a D/H value for BD +28° 4211 would be similar to that found for Feige 110 (Friedman et al. (2001) and γ^2 Vel (Sonneborn et al. 2000). However, a $\sim 40\%$ increase in $N(H\ I)$ would be inconsistent with the available spectra.

The D/O ratio for BD +28° 4211 appears to be high (Moos et al. 2001, Hébrard et al. 2001), arguing for $N(O\ I)$ as the anomalous quantity. Agreement with $\langle O/H \rangle_{ISM}$ would require a $\sim 40\%$

increase in $N(O\ I)$. One or more of the O I lines analyzed might actually be saturated, even though our analysis shows (Fig. 11) that the three O I lines are unsaturated. Line saturation, possibly as the result of narrow (cold gas) components would result in an underestimated column density. The effect of potential line saturation in $N(O\ I)$ was examined by excluding the strongest O I line ($\lambda 930$) from the fitting analysis, leaving only the two weaker O I lines. For this case we found $\log N(O\ I) = 16.28$, which is within 2σ of the best fit. We cannot determine whether this difference in N is the result of saturation, fixed pattern noise, LSF uncertainties, component structure, or some other cause. If this were the correct O I column density, the O/H ratio would be 2.72×10^{-4} , still well below $\langle O/H \rangle_{ISM}$ and $\langle O/H \rangle_{LB}$.

The N/H ratio toward BD +28° 4211 is $(5.08 \pm 1.66) \times 10^{-5}$ (2σ), a value that is marginally consistent with the mean ISM value of $N/H = (7.5 \pm 0.8) \times 10^{-5}$ (2σ) found for six OB stars by Meyer et al. (1997). However, the N II column density could be significant (see below). If so, then the N/H ratio toward BD +28° 4211 could well be consistent with the mean ISM result.

In the local ISM, the abundance of N I has been found to be reduced by ionization effects on some sight lines (Jenkins et al. 2000, Moos et al. 2001). N I has a photoionization cross section larger than that of H I and a large fraction of it can be ionized. There are only two N II transitions in the *FUSE* bandpass ($\lambda 915.6$ and $\lambda 1085.5$) and both of them are heavily saturated on all but the lowest column density sight lines. We derived a lower limit of $\log N(N\ II) > 14.2$ using both optical depth technique and profile fitting. Since we know that some N II is associated with the neutral component, we estimate an upper limit assuming that the b -value for N II is greater than that of the neutral gas. These assumptions give an upper limit of $\log N(N\ II) < 15.7$. We cannot rule out the possibility that an appreciable fraction of the nitrogen on the sight line toward BD +28° 4211 could be singly ionized.

Objects like the hot subdwarf BD +28° 4211 are important targets for studying D I and O I in the ISM with *FUSE* because they can sample regions of space beyond that accessible with white dwarfs ($d < 100$ pc) and closer than that sampled by the lightly-reddened O stars observable by *FUSE* ($d > 1$ kpc). Most of the nearer O stars far exceed the

FUSE brightness limit.

High-quality spectra of the type shown in Figures 1 and 2 are needed to understand these objects, and the observational techniques to obtain them with *FUSE* are now available. Over time issues like stellar continuum placement and stellar line identifications may be better understood, allowing even more precise interstellar abundance measurements.

This work is based on data obtained for the Guaranteed Time Team by the NASA-CNES-CSA *FUSE* mission operated by the Johns Hopkins University. Financial support to U. S. participants has been provided in part by NASA contract NAS5-32985 to Johns Hopkins University. Support for French participation in this study has been provided by CNES.

REFERENCES

- Audouze, J., & Tinsley, B. 1974, *ApJ*, 192, 487
- Bergeron, P., Wesemael, F., Beauchamp, A., Wood, M. A., Lamontagne, R., Fontaine, G., & Liebert, J. 1994, *ApJ*, 432, 305
- Bergeron, P., Wesemael, F., Lamontagne, R., & Chayer, P. 1993, *ApJ*, 407, L85
- Boesgaard, A. M., & Steigman, G. 1985, *ARA&A*, 23, 319
- Bohlin, R. C. 1986, *ApJ*, 308, 1001
- Bowers, C.W., et al. 1998, *Proc. SPIE*, 3356, 401
- Cardelli, J.A., Ebbets, D.C., & Savage, B.D. 1993, *ApJ*, 413, 401
- Friedman, S. D., et al. 2001, *ApJ*, submitted
- Gözl, M., et al. 1998, in *Proc. IAU Colloq. No. 166, The Local Bubble and Beyond*, eds. D. Breitschwerdt, M. J. Freyberg, J. Trümper (Berlin: Springer), 75
- Greenstein, J. L. 1952, *PASP*, 64, 256
- Haas, S., Dreizler, S., Heber, U., Jeffery, S., & Werner, K. 1996, *A&A*, 311, 669
- Hébrard, G., et al. 2001, *ApJ*, submitted
- Herbig, G. H. 1999, *PASP*, 111, 1144
- Howk, J.C., Savage, B.D., & Fabian, D. 1999, *ApJ*, 525, 253
- Hubeny, I., & Lanz, T. 1995, *ApJ*, 439, 875
- Jenkins, E. B. 1971, *ApJ*, 169, 25
- Jenkins, E. B. 1986, *ApJ*, 304, 739
- Jenkins, E. B., Joseph, C. L., Long, D., Zucchino, P. M., Carruthers, G. R., Bottema, M., & Delamere, W. A. 1988, in *UV Technology II*, ed. R. E. Huffman (Bellingham: International Society for Optical Engineering), 213
- Jenkins, E. B. et al., 2000, *ApJ*, 538, L81
- Jenkins, E.B., Tripp, T. M., Woźniak, P. R., Sofia, U. J., & Sonneborn, G. 1999, *ApJ*, 520, 182
- Kidder, K. M., Holberg, J. B., & Mason, P. A. 1991, *AJ*, 101, 579
- Kimble, R.A., et al. 1998, *ApJ*, 492, L83
- Kruk, J. W., et al. 2001, *ApJ*, submitted
- Landsman, W., & Bowers, C. 1997, in *HST Calibration Workshop with a New Generation of Instruments*, ed. S. Casertano, R. Jedrzejewski, C.D. Keyes, & M. Stevens (Baltimore: STScI), 132
- Lemke, M. 1997, *A&AS*, 122, 285
- Lemoine, M., et al. 2001, *ApJ*, submitted
- Linsky, J. L., 1998, *Sp. Sci. Rev.*, 84, 285
- MacRae, D. A., Fleischer, R., & Weston, E. B. 1951, *ApJ*, 113, 432
- Massey, P., & Gronwall, C. 1990, *ApJ*, 358, 344
- Massey, P., Strobel, K., Barnes, J. V., & Anderson, E. 1988, *ApJ*, 328, 315
- Meyer, D. M. 2001, in *XVIIth IAP Colloquium, Gaseous Matter in Galaxies and Intergalactic Space*, eds. R. Ferlet & M. Lemoine, in press
- Meyer, D. M., Cardelli, J. A., & Sofia, U. J. 1997, *ApJ*, 490, L103
- Meyer, D. M., Jura, M., & Cardelli, J. A. 1998, *ApJ*, 493, 222
- Moehler, S., Richtler, T., de Boer, K. S., Dettmar, R. J., & Heber, U. 1990, *A&AS*, 86, 53
- Moos, H. W., et al. 2000, *ApJ*, 538, L1
- Moos, H. W., et al. 2001, *ApJ*, submitted
- Morton, D. C., 1991, *ApJS*, 77, 119
- Nachman, P., Hobbs, L. M., 1973, *ApJ*, 182, 481
- Napiwotzki, R. 1993, *Acta Astron.*, 43, 343
- Napiwotzki, R. 1999, *A&A*, 350, 101

- Napiwotzki, R., & Rauch, T. 1994, *A&A*, 285, 603
- Napiwotzki, R., & Schönberner, 1993 in *White Dwarfs: Advances in Observation and Theory*, ed. M. A. Barstow, (Dordrecht: Kluwer), 99
- O'Meara, J. M., Tytler, D., Kirkman, D., Suzuki, N., Prochaska, J. X., Lubin, D., & Wolfe, A. M. 2001, *ApJ*, 552, 718
- Perryman, M. A. C., et al. 1997, *A&A*, 323, L49
- Rogerson, J. B., & York, D. G. 1973, *ApJ*, 186, L95
- Sahnou, D. J., et al. 2000, *ApJ*, 538, L7
- Savage, B. D. & Sembach, K. R. 1991, *ApJ*, 379, 245
- Savage, B. D. & Sembach, K. R. 1996, *ARA&A*, 34, 279
- Sfeir, D. M., Lallment, R., & Welsh, B. Y. 1999, *A&A*, 346, 785
- Sonneborn, G., Tripp, T. M., Forlet, R., Jenkins, E. B., Sofia, U. J., Vidal-Madjar, A., & Woźniak, P. 2000, *ApJ*, 545, 277
- Tosi, M., Steigman, G., Matteucci, F., & Chiappini, C. 1998, *ApJ*, 498, 226
- Verner, D. A., Barthel, P. D., Tytler, D. 1994, *A&A*, 108, 287
- Vidal-Madjar, A., & Gry, C. 1984, *A&A*, 138, 285
- Vidal-Madjar, A., et al. 1998, *A&A*, 338, 694
- Voit, M. 1997, *HST Data Handbook*, Vol. 1 (version 3; Baltimore: STScI)
- Walker, T. P., Steigman, G., Schramm, D. N., Olive, K. A., & Kang, H.-S. 1991, *ApJ*, 376, 51
- Werner, K. 1996, *ApJ*, 457, L39
- Wood, B. E., et al. 2001, *ApJ*, submitted
- Woodgate, B. E., et al. 1998, *PASP*, 110, 1183

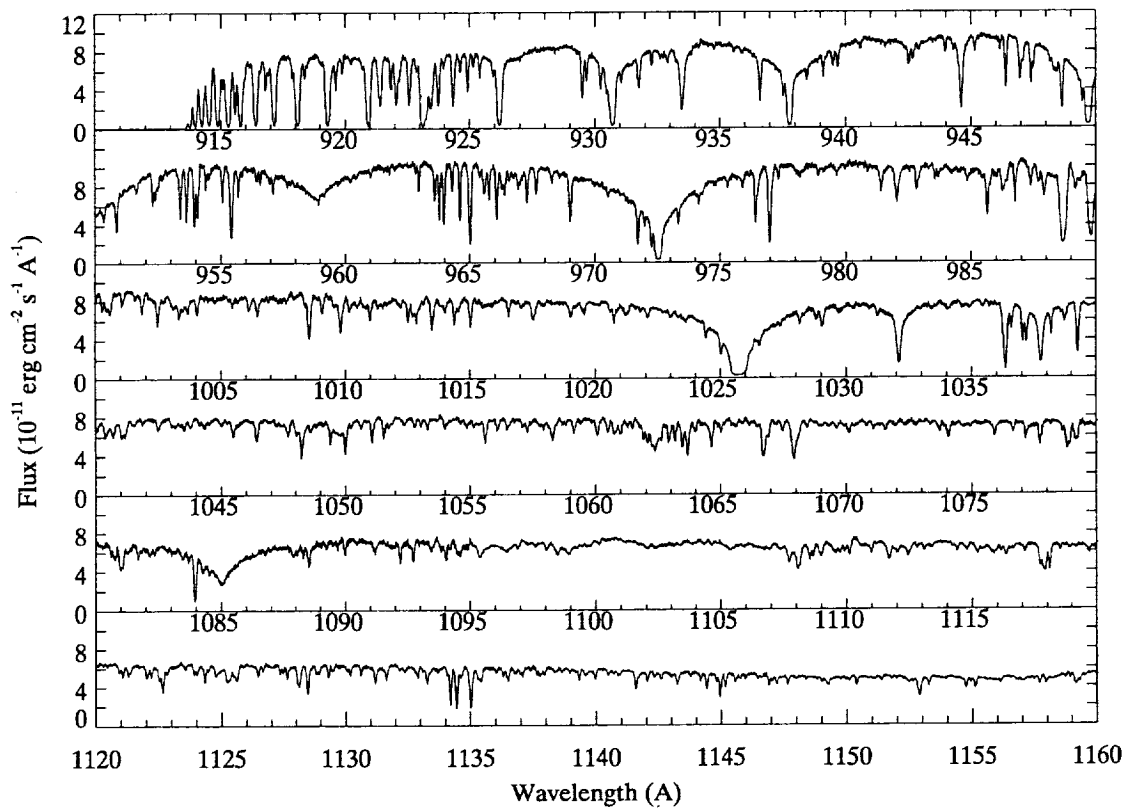


Fig. 1.— FUSE co-added LWRS spectra of BD +28° 4211 obtained on 2000 July 16. The spectral region 910-990 Å is from the SiC1 channel, 1000-1080 Å from LiF1, 1080-1095 Å from SiC2, and 1095-1160 Å from LiF1. The data have been binned by a factor of 2 for display purposes.

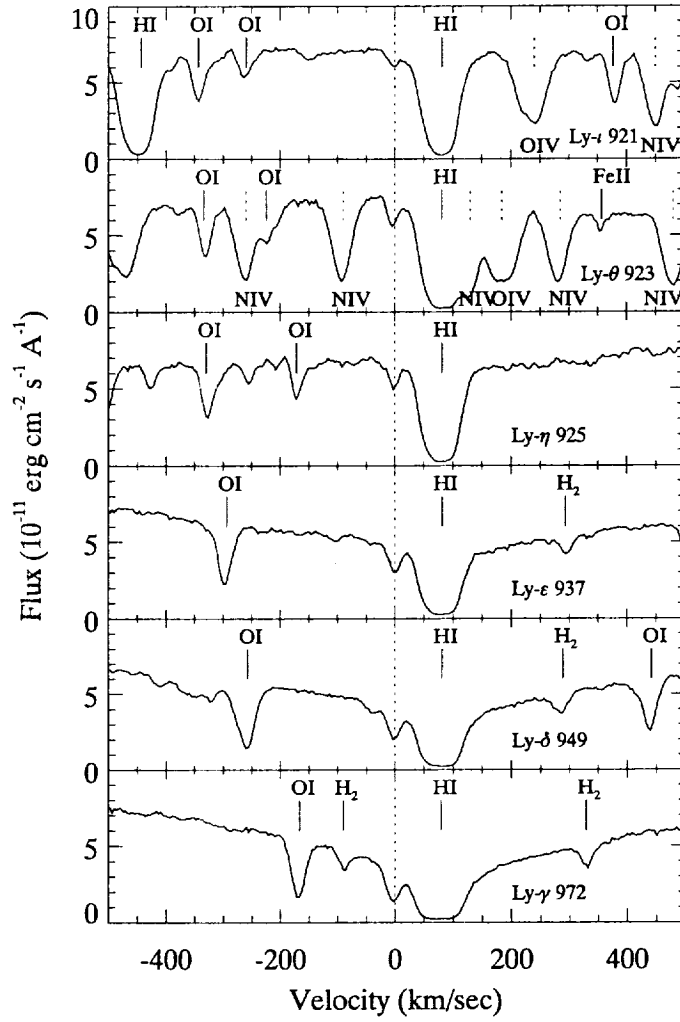


Fig. 2.— The higher Lyman lines in BD +28° 4211 from the SiC1 LWRs spectra are shown on a velocity scale. The zero point is set to the observed center of the D I feature. The principal interstellar atomic transitions are indicated above the spectrum and stellar transitions below.

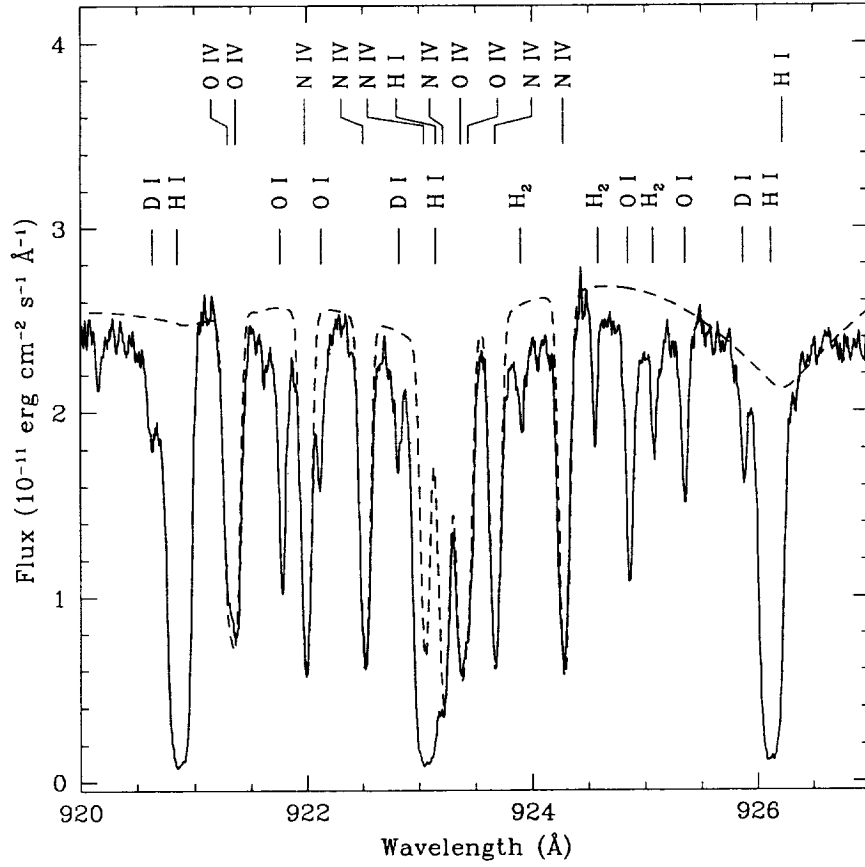


Fig. 3.— Comparison between a portion of the *FUSE* spectrum (solid line) and a synthetic spectrum (dashed line) computed with $T_{\text{eff}} = 82,000$ K, $\log(\text{He}/\text{H}) = -1.0$, $\log g = 6.2$, and incorporating solar nitrogen and oxygen abundances. The photospheric lines are labelled at the top of the figure. The ISM lines are labelled just above the spectrum.

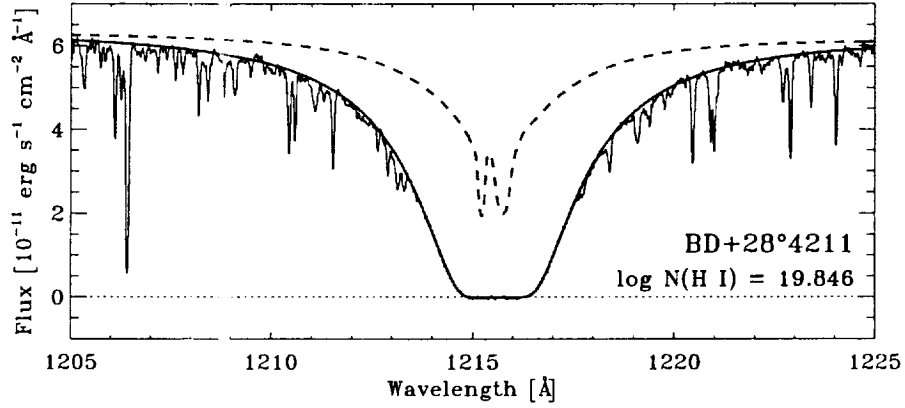


Fig. 4.— The wavelength region surrounding interstellar Ly α towards BD +28° 4211. The histogram shows the coadded STIS E140M observations of BD +28° 4211. The dashed gray line shows the adopted stellar model ($T_{eff} = 82,000$ K, $\log g = 6.2$, and $\log \text{He}/\text{H} = -1.0$) modified by a second order Legendre polynomial to bring it into agreement with the observed flux distribution. The two narrow absorption components in the stellar profile are the cores of H I and He II. The solid line shows the best-fit H I model times this stellar continuum. The best-fit interstellar parameters are $v_{hel} = -13.3 \pm 0.8$ km s $^{-1}$ and $\log N(\text{H I}) = 19.846^{+0.034}_{-0.036}$ (both 2σ uncertainties).

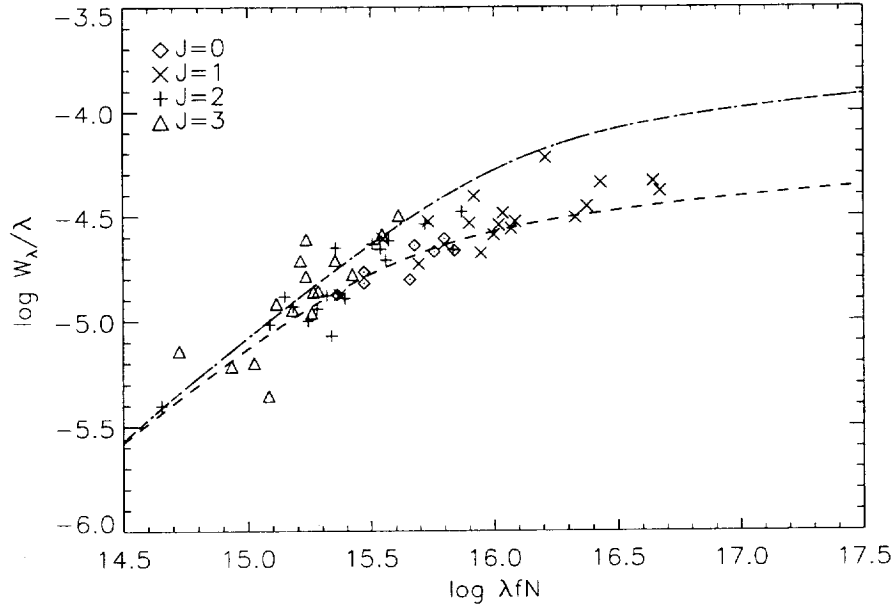


Fig. 5.— Curve of growth for H_2 with fits corresponding to $b = 2.8 \text{ km s}^{-1}$ (dashed line) and $b = 8.5 \text{ km s}^{-1}$ (dot-dashed line), which were the minimum and maximum b values found in the fit of the individual rotational levels. The 1σ error bars are comparable to the scatter in the W_λ measurements. They were omitted from the figure for clarity.

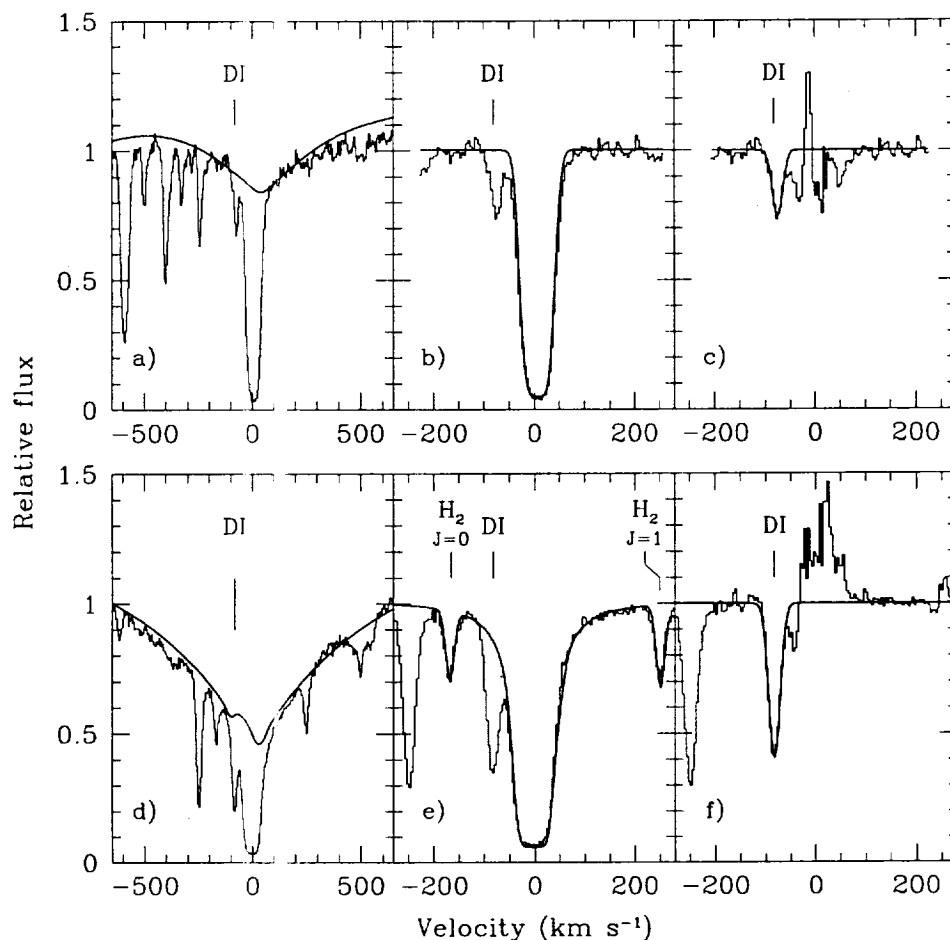


Fig. 6.— Continuum normalization for D I W_λ measurements. Panels a) - c) illustrate the method used to measure W_λ of D I $\lambda 925.974$ ($1, \eta$) in the SiC2 channel and LWRs aperture. Panel a) shows the stellar model placement (smooth, solid line) over the data (histogram-style line). Panel b) shows the ISM model (H I + H₂ only) relative to the spectrum normalized by the stellar model. Panel c) shows the ISM-normalized spectrum from b) and the Gaussian fit to the D I Ly η profile used to measure the area of the line under the continuum. The red side of the reconstructed D I profile is affected by large residuals from dividing by the near-zero flux in the core of H I. Panels d)-f) show the same method applied to D I Ly γ in the same channel and aperture. The weak feature in the blue wing of the stellar Ly γ model profile (panel d) is He II, while the stronger feature directly below it in the observed spectrum is interstellar D I.

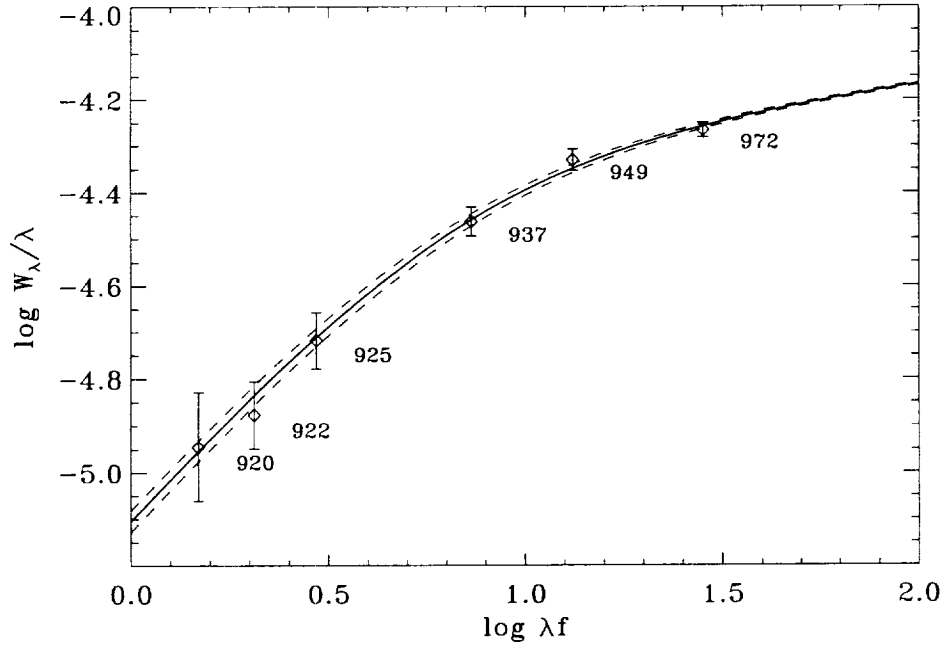


Fig. 7.— The best fit curve of growth for D I (solid line) corresponding to $\log N(\text{D I}) = 14.99 \pm 0.10$ (2σ) and $b = 5.2 \text{ km s}^{-1}$. The dashed lines are the 1σ errors in the fit. The equivalent width data points, shown with the wavelength of the transition and 1σ error bars, are the weighted average of W_λ from the SiC1 and SiC2 channels and the LWRS and MDRS observations.

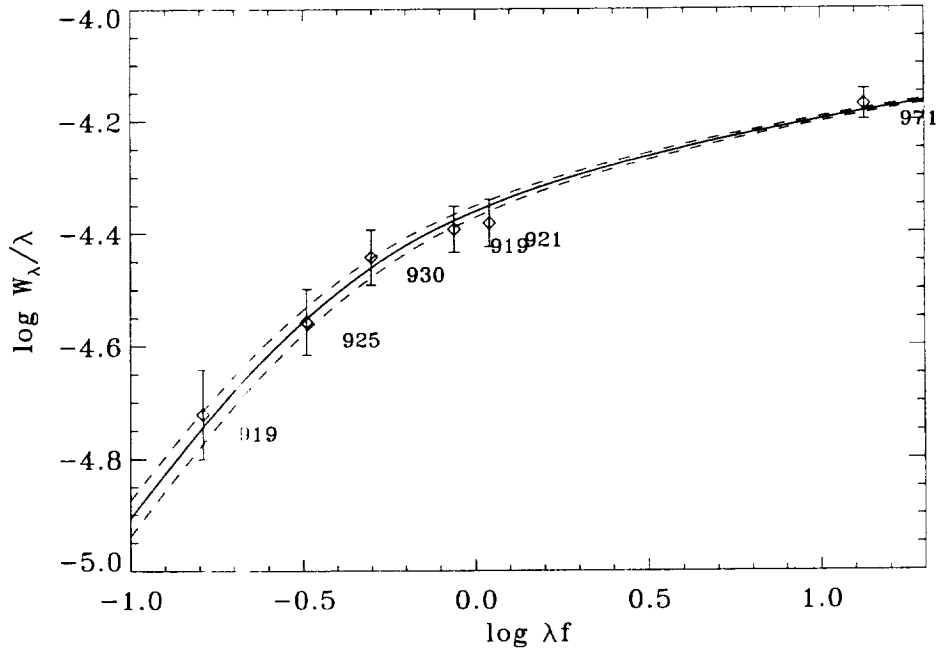


Fig. 8.— The best fit curve of growth for O I (solid line) corresponding to $\log N(\text{O I}) = 16.23 \pm 0.08(2\sigma)$ and $b = 4.46 \text{ km s}^{-1}$. The dashed lines are the 1σ errors in the fit. The equivalent width data points, shown with the wavelength of the transition and 1σ error bars, are the weighted average of W_λ from the SiC1 and SiC2 channels and the LWRS and MDRS apertures.

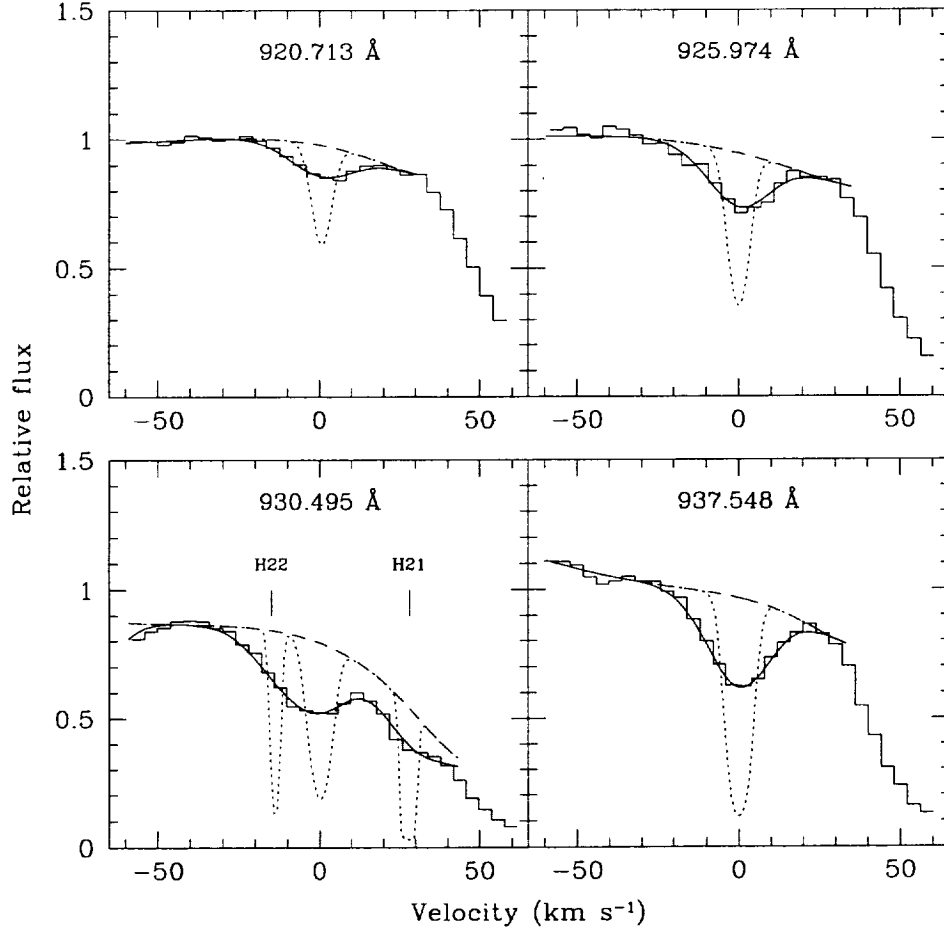


Fig. 9.— The fits of D I Ly ϵ λ 937.5, Ly ζ λ 930.5, Ly η λ 926.0, and Ly ι λ 920.7 for the SiC2 channel and LWRS aperture are shown on a relative velocity scale. The histogram lines represent the data, the thick solid lines are the final fits to the spectrum, and the dashed lines are the fits after deconvolution with the LSF. Note that no D I lines stronger than Ly ϵ were used since this transition is already optically thick ($\tau_0 \sim 2$). Note also D I Ly ζ is blended with H₂($J = 1$) and H₂($J = 2$). The profile fitting technique recovers the information for the D I profile contained in the data.

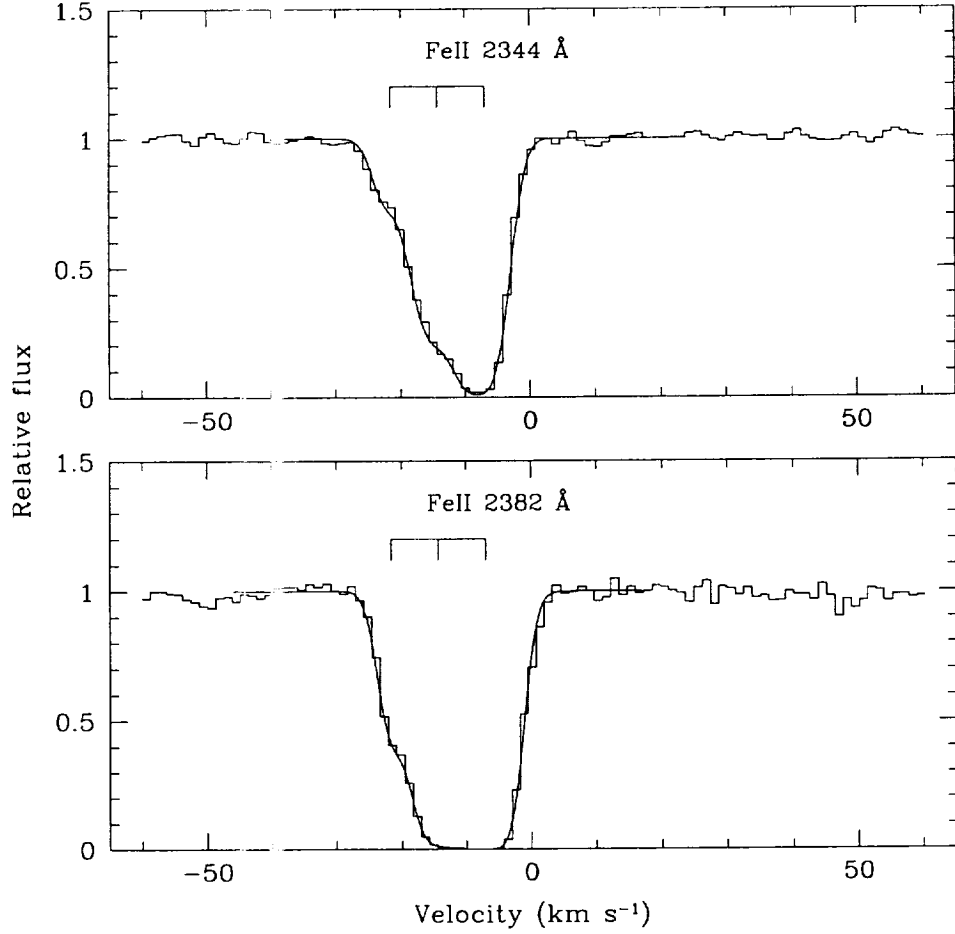


Fig. 10.— Fe II $\lambda 2344$ and $\lambda 2382$ line profiles from *HST*/STIS E230H spectra of BD +28° 4211 are compared with the best fit model and shown on a heliocentric velocity scale. The smooth solid line is the best fit obtained with three components. The histogram line is the normalized spectrum. 70% of the total column density is in the dominant component (right), 27% in the middle component, and 3% in the weakest component (left). The two stronger components are separated by less than 8 km s⁻¹ and are not resolved in Fe II features present in the *FUSE* spectra of BD +28° 4211.

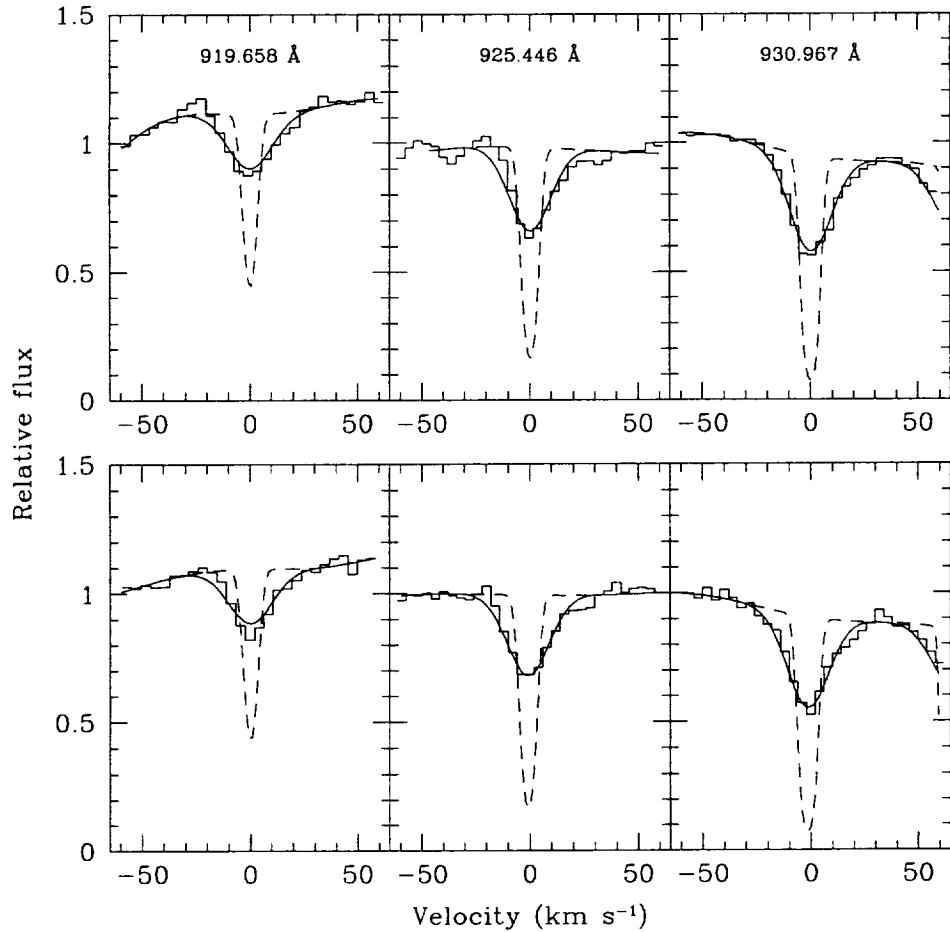


Fig. 11.— Profile fits to three optically thin O I lines ($\lambda\lambda 919.92, 925.45$, and 930.26). The top panels shows the fits for the SiC2 channel LWRs aperture spectra. The bottom panel shows the same transitions for the same channel but MDRS aperture. The definitions of the different line styles are the same as Figure 9. Both data sets are very similar, with a LSF $FWHM \sim 20 \text{ km s}^{-1}$ for LWRs and $\sim 18 \text{ km s}^{-1}$ for MDRS.

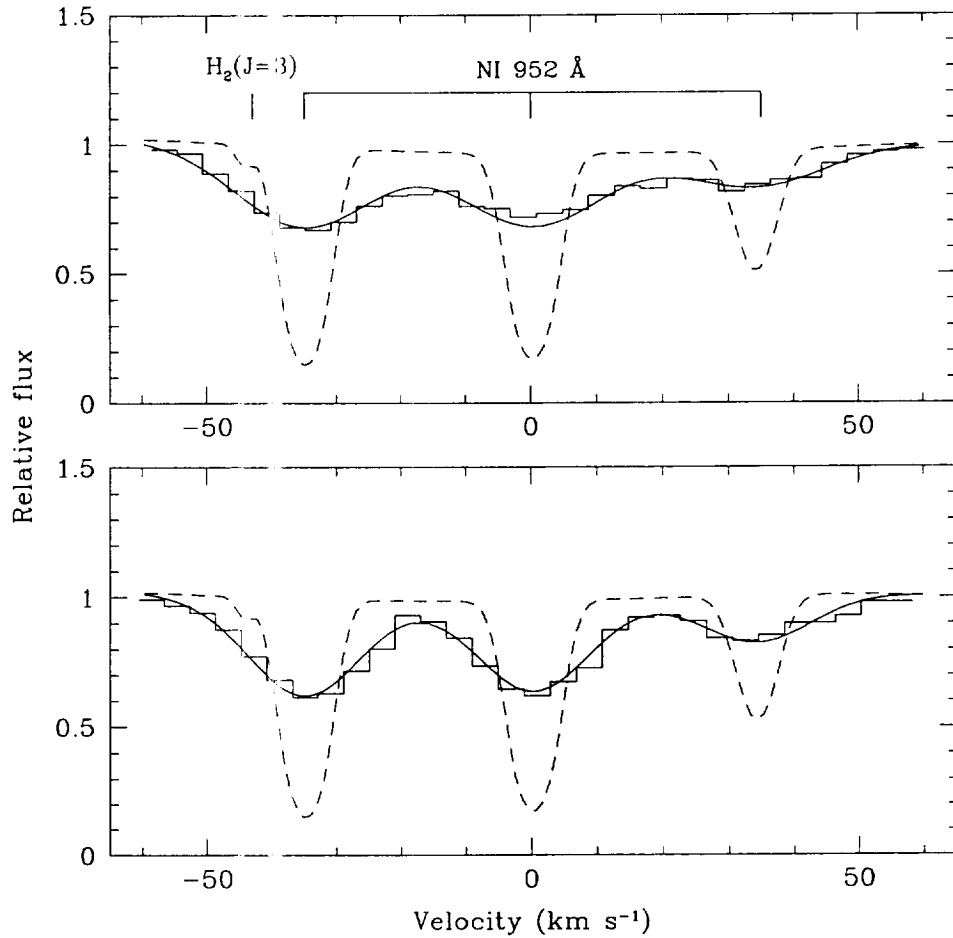


Fig. 12.— Profile fits to the Ni 952 multiplet. The top panels shows the fits to the spectrum for the SiC2 channel and the LWRS aperture. The bottom panel is the same channel for the MDRS aperture. The definitions of the different line styles are the same as Figure 9. The spectral resolution in the two data sets are very similar. Note the H₂ L14 – 0 P(3) line on the blue side of the triplet. This Ni triplet is the only one available in the *FUSE* bandpass that is not optically thick and free of significant interference by lines of other species.

TABLE 1
FUSE OBSERVATIONS OF BD +28° 4211

Program ID	Date	Aperture	FP-split pos No.	Offset (pixels)	$\Delta\lambda$ (Å)	Exposures	Exp. Time (s)
M1080901	Jun 13 2000	LWRS	1–4	2192
M1040101	Jul 16 2000	LWRS	1	−27	−0.17	1–14	6251
			2	0	0.00	14–25	5073
			3	+7	+0.04	26–30	2454
			4	+36	+0.23	31–36	2799
M1040105	Sep 19 2000	LWRS	3	+7	+0.04	1–8	3691
			4	+36	+0.23	9–17	4146
M1040102	Jul 17 2000	MDRS	1	−12	−0.08	1–13	6279
			2	0	0.00	14–30	8211
			3	+5	+0.03	31–42	5795
			4	+12	+0.08	43–52	4540

TABLE 2
PROPERTIES OF BD +28° 4211

Quantity	Value	Reference
Spectral Type	sdO	1
l	81.87°	2
b	−19.29°	2
d^a (pc)	104 ± 18	2
V	10.53	3
$U - B$	−1.26	3
$B - V$	−0.34	3
v_{hel}	+20.2 ± 0.8 km s ^{−1}	4
T_{eff} (K)	82,000	1
log g (cm s ^{−2})	6.2	1
log(He/H)	−1.0	1

^aTrigonometric parallax

REFERENCES.—(1) Napiwotzki 1993; (2) Perryman et al. 1997; (3) Kidder et al. 1991; (4) This paper (§4).

TABLE 3
H₂ COLUMN DENSITIES^a

J	No. Lines	$\log(N(\text{H}_2))$
0	4	$14.57^{+0.45}_{-0.15}$
1	8	$14.76^{+0.16}_{-0.06}$
2	13	$14.39^{+0.07}_{-0.04}$
3	14	$14.17^{+0.05}_{-0.03}$
4	3	< 13.68

^aErrors are 2σ . Value for $J = 4$ is a 3σ upper limit.

TABLE 4
D I AND O I EQUIVALENT WIDTHS^a

Line	λ (Å)	$\log f\lambda$	W_λ (LWRS) (mÅ)		W_λ (MDRS) (mÅ)		$\langle W_\lambda \rangle$ (mÅ)
	D I		SiC1	SiC2	SiC1	SiC2	
Ly ι	920.713	0.17	...	10.4 ± 4.7	...	10.5 ± 4.4	10.5 ± 3.2
Ly κ	922.899	0.31	14.1 ± 6.0	13.7 ± 3.8	10.9 ± 3.0	...	12.3 ± 2.2
Ly η	925.974	0.47	18.5 ± 7.5	18.3 ± 7.0	19.8 ± 5.0	16.0 ± 4.0	17.7 ± 2.7
Ly ϵ	937.548	0.86	34.4 ± 5.0	30.3 ± 5.7	34.1 ± 4.0	29.1 ± 5.0	32.3 ± 2.4
Ly δ	949.485	1.12	42.0 ± 4.6	43.8 ± 4.4	48.5 ± 5.0	44.0 ± 5.5	44.4 ± 2.4
Ly γ	972.272	1.45	50.6 ± 4.0	55.0 ± 4.4	52.3 ± 3.0	54.6 ± 5.0	52.8 ± 1.9
	O I		SiC1	SiC2	SiC1	SiC2	
	919.917 ^b	-0.79	15.6 ± 1.2	20.8 ± 1.2	16.7 ± 1.3	16.6 ± 1.3	17.5 ± 0.6
	925.446 ^b	-0.49	27.4 ± 1.3	23.7 ± 1.3	28.1 ± 1.4	23.1 ± 1.3	25.7 ± 0.7
	930.257 ^b	-0.30	32.5 ± 1.4	34.0 ± 1.4	34.8 ± 1.5	33.1 ± 1.4	33.6 ± 0.7
	919.658 ^c	-0.06	34.5 ± 1.3	41.5 ± 1.4	43.1 ± 1.4	30.9 ± 1.3	37.2 ± 0.7
	921.857 ^c	0.04	41.7 ± 1.4	37.6 ± 1.4	41.3 ± 1.5	33.4 ± 1.4	38.3 ± 0.7
	971.738 ^c	1.13	64.5 ± 1.5	65.3 ± 1.5	68.6 ± 1.6	63.6 ± 1.5	65.4 ± 0.8

^aErrors in this table are 1σ .

^bSinglet. Used f -values from Morton (1991).

^cTriplet. Used sum of f -values from Morton (2000, private communication).

TABLE 5
 $N(\text{O I})$ FROM CURVE OF GROWTH^a

Channel	Aperture	$\log(N(\text{OI}))$ (cm^{-2})	b (km s^{-1})
SiC1	LWRS	16.22 ± 0.10	4.46
SiC1	MDRS	16.25 ± 0.06	4.83
SiC2	LWRS	16.29 ± 0.16	4.41
SiC2	MDRS	16.18 ± 0.18	4.24

^aErrors in this table are 2σ .

TABLE 6
 D I , N I , AND O I PROFILE FITTING RESULTS^a

Case	No. Windows	DOF	χ^2_{min}	b (km s^{-1})	$\log N(\text{D I})$ (cm^{-2})	$\log N(\text{N I})$ (cm^{-2})	$\log N(\text{O I})$ (cm^{-2})
Case 1 ^b	39	1444	1674	4.0	14.99 ± 0.05	15.51 ± 0.05	16.22 ± 0.09
Case 2 ^c	39	1405	1441	4.2	14.99 ± 0.07	15.57 ± 0.09	16.22 ± 0.16
Case 3 ^d	41	1527	1929	$3.8 + 3.3$	14.96 ± 0.05	15.49 ± 0.05	16.17 ± 0.06

^aErrors in this table are 2σ .

^bOne Gaussian component, LSF fixed for each channel (SiC1 or SiC2).

^cOne Gaussian component, LSF free to vary from window to window.

^dThree Gaussian components as defined by Fe II velocity structure, LSF fixed for each channel (SiC1 or SiC2). See text.

TABLE 7
 D I , N I , AND O I COLUMN DENSITIES ^a

Ion	Profile Fitting	Mean COG	Adopted Solution
$\log(N(\text{D I}))$ (cm^{-2})	14.99 ± 0.03	14.99 ± 0.10	14.99 ± 0.05
$\log(N(\text{N I}))$ (cm^{-2})	15.55 ± 0.13	...	15.55 ± 0.13
$\log(N(\text{O I}))$ (cm^{-2})	16.21 ± 0.10	16.23 ± 0.08	16.22 ± 0.10

^aErrors in this table are 2σ .

TABLE 8
INTERSTELLAR ABUNDANCE TOWARD BD +28° 4211^a

Quantity	Value
$\log N(\text{D I})$	$14.99 \pm 0.05 \text{ cm}^{-2}$
$\log N(\text{N I})$	$15.55 \pm 0.13 \text{ cm}^{-2}$
$\log N(\text{O I})$	$16.22 \pm 0.10 \text{ cm}^{-2}$
$\log N(\text{H I})$	$19.846^{+0.036}_{-0.034} \text{ cm}^{-2}$
D/H	$1.39 \pm 0.21 \times 10^{-5}$
N/H	$5.08 \pm 1.66 \times 10^{-5}$
O/H	$2.37 \pm 0.55 \times 10^{-4}$
D/N	0.274 ± 0.092
D/O	0.0590 ± 0.0133

^aErrors in this table are 2σ .

